Published in final edited form as:
Invest Ophthalmol Vis Sci. 2008 May ; 49(5): 2103–2119. doi:10.1167/iovs.07-0980.

Changes in Cellular Structures Revealed by Ultra-high Resolution Retinal Imaging in Optic Neuropathies

Stacey S. Choi[1], **Robert J. Zawadzki**[1], **John L. Keltner**[1,2], and **John S. Werner**[1]

[1]Department of Ophthalmology & Vision Science, University of California Davis, Sacramento, California.

[2]Department of Neurology and Neurological Surgery, University of California Davis, Sacramento, California.

Abstract

PURPOSE—To study the integrity of inner and outer retinal layers in patients with various types of optic neuropathy by using high-resolution imaging modalities.

METHODS—Three high-resolution imaging systems constructed at the University of California Davis were used to acquire retinal images from patients with optic neuropathy: (1) adaptive optics (AO)-flood–illuminated fundus camera, (2) high-resolution Fourier domain optical coherence tomography (FDOCT), and (3) adaptive optics-Fourier domain optical coherence tomography (AO-FDOCT). The AO fundus camera provides en face images of photoreceptors whereas cross-sectional images (B-scans) of the retina are obtained with both FDOCT and AO-FDOCT. From the volumetric FDOCT data sets, detailed thickness maps of a three-layer complex consisting of the nerve fiber (NF), ganglion cell (GC), and inner plexiform (IP) layers were created. The number of visible cones in the en face images of photoreceptors was then compared with visual sensitivity maps from Humphrey visual field (HVF; Carl Zeiss Meditec, Inc., Dublin, CA) testing, as well as FDOCT and AO-FDOCT images, including the thickness maps of the NF–GC–IP layer complex. Five types of optic neuropathy were studied: (1) optic neuritis with multiple sclerosis (MS), (2) idiopathic intracranial hypertension (pseudotumor cerebri), (3) nonarteritic anterior ischemic optic neuropathy (NAION), (4) optic nerve head drusen with NAION, and (5) systemic lupus erythematosus with MS and arthritis.

RESULTS—With permanent visual field loss and thinning of the NF–GC–IP layer complex, cone photoreceptors showed structural changes, making them less reflective, which caused the appearance of dark spaces in the en face images (hence, reduced number of visible cones) and indistinct outer retinal layers in OCT images. However, when the visual field loss was only transient, with a normal NF–GC–IP layer complex, there were no detectable abnormalities in cone photoreceptors (i.e., they were densely packed and had distinct photoreceptor layering in the OCT images).

CONCLUSIONS—Cone photoreceptors show structural changes when there is permanent damage to overlying inner retinal layers. There was a positive relation between the thickness of the three-layer inner retinal complex, visual sensitivity, and integrity of the cone mosaic.

The most common optic neuropathies in adults, besides glaucoma, are optic neuritis (ON) and nonarteritic anterior ischemic optic neuropathy (NAION) with yearly incidences of 5.1/100,000 and 2.3/100,000, respectively, in industrialized countries.[1,2] The etiology of NAION is believed to be ischemia, caused by disruption of blood flow to the capillaries of the

Corresponding author: Stacey S. Choi, Department of Ophthalmology & Vision Science, 4860 Y St., Suite 2400, University of California Davis, Sacramento, CA 95817; E-mail: sschoi@ucdavis.edu.

Disclosure: **S.S. Choi**, None; **R.J. Zawadzki**, None; **J.L. Keltner**, None; **J.S. Werner**, None

optic nerve head,[3] whereas in ON, it is thought to be demy-elination, where the integrity of the blood-brain barrier in the optic nerve head is disrupted.[4]

Although NAION and ON have different etiologies, both are associated with loss of ganglion cell axons.[3,5] It has been shown that the axons undergo degeneration at the disc, either from inflammation in ON or ischemia in NAION and then anterograde degeneration results in optic atrophy and ganglion cell death. Other less prevalent optic neuropathies, such as optic nerve head drusen and compressive optic neuropathy have also shown disc pallor and thinning of nerve fiber layer (NFL).[6–9]

Common visual symptoms in various types of optic neuropathy are loss of visual acuity, impaired contrast sensitivity, decreased color discrimination, and visual field defects.[10–22] It has been assumed that loss of vision and color vision in optic neuropathy are mainly due to axonal damage. However, several glaucoma studies have presented evidence of photoreceptor involvement in conjunction with retinal ganglion cell (RGC) damage.[23–25] Our recent study on glaucoma revealed that there are structural changes in cone photoreceptors, together with expected inner retinal changes, which raises the possibility that several other optic neuropathies have upstream changes in the outer retina.[26] The purpose of this article is to examine this issue through high-resolution in vivo retinal imaging of patients with various types of optic neuropathy.

METHODS

Subjects

Six patients with several different types of optic neuropathy were tested. The patients included two with multiple sclerosis (MS), one with bilateral NAION, one with bilateral optic nerve head drusen with NAION, one with idiopathic intracranial hypertension (pseudotumor cerebri), and one case of systemic lupus erythematosus with MS. The diseases were diagnosed in these patients based on clinical examinations, including fundus examination, visual field analysis, and Stratus OCT imaging (Carl Zeiss Meditec, Inc., Dublin, CA). The clinical findings in the patients are summarized in Table 1. Both eyes were tested in three of six patients. In those cases in which only one eye was tested, the eye that exhibited the worse visual field was chosen for study. All subjects ranged in age from 34 to 57 years with refractive error ≤ -3.5 D for spherical and < -0.75 D for astigmatic corrections. Four normal subjects of various ages (21, 35, 45, and 55 years) were also recruited for direct comparison. All were screened with comprehensive ophthalmic examinations including dilated fundus examination and fundus photographs, to verify that they were free of retinal and optic nerve disease. They were also free of any systemic diseases and had low refractive error (i.e., < -3.5 D for spherical and < -0.5 D for astigmatic corrections). Refractive error was corrected with trial lenses before AO retinal imaging. The tenets of the Declaration of Helsinki were observed, and written informed consent was obtained after all procedures were fully explained and before any experimental measurements were performed.

Procedure

In Vivo Retinal Imaging—Three high-resolution imaging systems were used to acquire retinal images from the same retinal locations in each patient. Each instrument provides complementary information. The AO-flood–illumination system has high lateral resolution and provides en face images of cone photoreceptors from which cone density can be measured. The term cone density is used to reflect the number of cones that are visible in the image. FDOCT has high axial resolution and a relatively large field of view. AO-FDOCT has high lateral and high axial resolution, but a smaller field of view in its current configuration. FDOCT and AO-FDOCT were used to acquire cross-sectional images at the corresponding retinal

locations so that direct comparisons could be made between the en face and cross-sectional images from the same retinal location. Furthermore, FDOCT images allow creation of precise thickness maps of various retinal layers that can be used to monitor, detect, and measure micrometer-level changes in thickness.

Owing to the size of the cellular structures of interest (only a few micrometers), the motion artifacts that can easily be overlooked in other conventional imaging systems become a major hindrance in high-resolution imaging, from the acquisition and processing aspects. To minimize these motion artifacts, a bite bar and/or a forehead rest are used during imaging, and also all the images are registered offline not only to enhance the contrast but also to bring out the details in the image more clearly. The use of a bite bar/forehead rest and image registration has become an integral part of high-resolution imaging, and they have proven to be effective.

AO-Flood–Illumination System: A detailed description of the imaging system and the procedures have been published elsewhere.[27] Briefly, the pupil was dilated with a combination of 1% tropicamide and 2.5% phenylephrine. During testing, the subject's head and eye movements were minimized by using a bite bar with a dental impression. The imaging locations were selected based on the Humphrey visual field (HVF; Carl Zeiss Meditec, Inc.) test results from which areas of different visual sensitivity could be identified. The residual aberrations after trial lens correction were measured with a Shack-Hartmann-based wavefront sensor and then corrected with a deformable mirror (DMs; Itek Optical Systems, Lexington, MA) having 109 actuators with a ±2-μm mirror stroke. The imaging wavelength was 650 ± 40 nm, and the size of each AO image subtended 1° on the retina. The lateral resolution of the system is ~2.5 μm, which allows visualization of individual cone photoreceptors. Seven to eight AO images were registered and averaged, to improve the signal-to-noise ratio of the image by approximately three times. To ensure that all the images that are selected for image registration are sharp and free of any eye motion, each image was visually inspected before registration. The registration was performed based on normalized cross correlations between the chosen reference image and subsequent images. The images were then shifted and rotated accordingly to achieve the best overlap with the reference image. All registered images were acquired within the same session under identical conditions. Therefore, no correction was necessary for different magnification between images.

Stiles-Crawford Effect Imaging: Similar to the technique used by Roorda and Williams,[28] the entrance position of the imaging light in the AO-flood–illuminated fundus camera was varied in 1-mm increments along the horizontal meridian of the dilated pupil, to assess the angular tuning of cone photoreceptors based on the Stiles-Crawford effect (SCE).[29] For each entrance position, a series of images was acquired and registered to determine whether any particular entrance position revealed cones that were not previously visible with the central entrance position.

Fourier Domain OCT: FDOCT images were obtained by using a laboratory instrument described in detail elsewhere.[30–32] Briefly, a superluminescent diode at 855 ± 33 nm was used to acquire B-scans (6 × 2 mm, 1000 A lines, line exposure time [τ], 80 μs; frame acquisition rate, 12 frames/s) and volumes (6 × 6 × 2 mm, 100 frames; acquisition time, 9 seconds) of the retina. Consecutive B-scans permitted structural changes to be identified in any of the retinal layers, whereas volumetric data sets were used to create thickness maps of the inner retinal layers.[32] This system has an axial resolution of ~4.5 μm (i.e., more than two times higher resolution than Stratus OCT; Carl Zeiss Meditec, Inc.) and a lateral resolution of ~15 μm. Before imaging, the pupil was dilated as described earlier. A bite bar and a forehead rest were used to stabilize movements of the head during imaging. To reduce motion artifacts in volumetric data, individual B-scans were registered to improve axial and transverse alignment of the consecutive frames.[33]

Adaptive Optics-FDOCT: Highly magnified and detailed volumetric cross-sectional images of the retina (0.5 × 0.5 mm, 500 A lines; τ, 50 μs; frame acquisition rate, 36 frames/s with 250 frames), subtending ~1.7° on the retina, were acquired with an AO-FDOCT system with a superluminescent diode (SLD) at 841 ± 25 nm. A detailed description of the system and the procedure for imaging have been published elsewhere.[34] Briefly, the pupil was dilated and the eye's aberrations were measured and corrected by a Shack-Hartmann wavefront sensor and DMs, respectively. The AO-FDOCT system uses two DMs: a bimorph DM with a ± 16-μm mirror stroke and a microelectro-mechanical systems (MEMS) DM with ± 0.75-μm mirror stroke. The bimorph DM was used to correct the refractive error, and the MEMS DM was used to correct the residual higher-order aberrations. To stabilize the patient's head, a bite bar with dental impression and a forehead rest were used during imaging. Each system mentioned has a calibrated internal fixation target for different retinal eccentricities, so that the same retinal location on each patient would be imaged by these three separate imaging systems.

Image Analysis

Cone Density Measurement and Identification of Cones: Cone density was calculated from the AO-flood en face images by using a custom software (MatLab; The Mathworks, Inc., Natick, MA) program that automatically identifies cones based on the peak intensity and diameter.[35] Algorithm details are published else-where.[35] Briefly, the user identifies and measures the dimmest and the brightest cones in each image as well as the shortest center-to-center spacing between adjacent cones. Then these values are used as a threshold for selecting cones in the image. The algorithm selects only pixels that satisfy both conditions: (1) the intensity lies between the min and max threshold values; and (2) the spacing must exceed the threshold. If there are blood vessels in the image, they are traced, and their area is subtracted from the image area before the cone density calculation, as it will otherwise underestimate the number of visible cones in the image. The accuracy of this algorithm has been tested using both simulated and real retinal images from normal subjects, and was found to be in 97.7% agreement with the simulated images and within 1 SE of the mean density in Curcio et al.[36] for the real retinal images. The cone counts from our images were compared to the histology data reported by Curcio et al. at the corresponding retinal locations to calculate relative cone density. We[35] and others[37,38] have demonstrated elsewhere that there is a close agreement between cone densities in AO en face images and the histology data for normal retina.

SCE Images: Cones were identified using the same software program mentioned earlier (MatLab; The MathWorks). Those cones that became visible under SCE imaging conditions were manually labeled (Photoshop, ver. 8; Adobe Systems, Inc., San Jose, CA).

Quantification of Inner Retinal Layer Thickness with FDOCT: From the 3-D volumes of the retina, a three-layer complex including the NFL, ganglion cell layer (GCL), and inner plexiform layer (IPL) was isolated to create a two-dimensional thickness map. To extract retinal layers, a machine learning support vector machine (SVM) algorithm that allows the semiautomatic segmenting of different retinal structures was used.[32] When the NFL, GCL, or both are absent or thin due to optic neuropathy, it becomes difficult to segment the individual layers accurately; therefore, the IPL was included in all cases, to make the segmentation more reliable.

RESULTS

In Vivo Imaging of Inner and Outer Retinal Layers

As a reference, images of a normal retina obtained with our high-resolution imaging systems are shown in Figure 1. Figure 1a shows an en face image of cone photoreceptors (FOV = ~1°) taken with the AO-flood–illuminated fundus camera. As expected at 4° temporal retina, the

cone photoreceptors are more densely packed than at more eccentric retinal locations. Darker areas in the image represent shadows cast by blood vessels located above the photoreceptors. Figure 1b shows corresponding B-scans, obtained with the FDOCT, through the fovea and six other retinal locations in two subjects. B-scans were obtained at 6° superior retina, 4° superior retina, 2° superior retina, the fovea, 2° inferior retina, 4° inferior retina, and 7° inferior retina. The NFL is much thicker on the nasal aspect of the fovea than on the temporal side. Figure 1c shows AO-FDOCT images (0.5 × 0.5 mm) acquired at six different retinal locations in the same subjects. These locations are shown on the fundus photograph of each eye. Another normal AO-FDOCT image (0.5 × 0.5 mm) taken at 4.5° temporal retina is shown for labeling purposes. The normal photoreceptor layer is identifiable as four well-defined stratified layers as shown in Figure 1c. The top layer represents the external limiting membrane (ELM; labeled 1); the first bright, interrupted line represents the junction between the inner and outer segments of cone photoreceptors (IS/OS; labeled 2); the second bright, interrupted line is thought to be the junction where the outer segments of cone photoreceptors are enveloped by the retinal pigment epithelium (OS/RPE), also named Verheoef's membrane (labeled 3); and the bottom bright, thicker line represents the RPE. Each interruption in the IS/OS and OS/RPE layers represents a gap between adjacent cones.

For each of the six optic neuropathy cases, AO-flood en face images of cone photoreceptors and OCT images from the same retinal locations were examined and compared. Each box on the FDOCT images denotes the retinal location where the corresponding AO-flood en face image was taken. Because of space limitations, all the FDOCT images (Supplementary Fig. S1–Supplementary Fig. S5, Supplementary Fig. S7) are online at http://www.iovs.org/cgi/content/full/49/5/2103/DC1. The percentage underneath each AO-flood en face image refers to the cone density compared with the histology data.[36]

Case 1: NAION—A 57-year-old man with bilateral NAION was tested. Both eyes showed significant optic atrophy with marked constriction of visual fields.

AO-flood en face images of cone photoreceptors were acquired in both eyes at three retinal locations having different visual sensitivity. Figures 2a and 2b show the cone mosaic of each eye at retinal locations shown on the HVF plot. Because of the severity of the visual field defect, the standard stimulus (size III) was not sensitive enough to plot a meaningful visual field, therefore, a larger stimulus (size V) was used instead. Figure 2a shows dark spaces in the cone mosaic images where cones were not visible at all three retinal locations. At 2° temporal-2° inferior retina and 2° temporal-2° superior retina, the cone density was reduced to 56% and 62% of normal, respectively, and at 4° nasal-4° superior retina, where the visual sensitivity was found to be higher than in the other two locations, the cone density was 79%. The left eye showed the same trend as the right eye (Figure 2b; i.e., dark spaces were evident in the cone mosaic images, and their extent increased with decreasing HVF sensitivity). At the retinal locations where sensitivity was more reduced (i.e., 4° temporal-7° superior retina and 4° temporal-4° superior retina), the cone density was 53% and 61%, respectively, and at the location where higher sensitivity was registered (i.e., 4° nasal-4° superior retina) the cone density was maintained at 83%. Some examples of these dark spaces in the cone mosaic are denoted by arrows in Figure 2.

Supplementary Figure S1a shows FDOCT B-scans through the same three vertical eccentricities from the fovea in the right eye. It is striking to note that the NFL was barely visible across the entire scan at these locations and the photoreceptor OS/RPE junction appeared mottled and blurred, especially at 2° temporal-2° superior retina and 2° temporal-2° inferior retina. Supplementary Figure S1b shows the FDOCT images at the corresponding vertical locations in the left eye. The B-scan image through 7° superior retina from the fovea revealed almost no NFL across the entire scan. This is the eccentricity that includes the retinal

location with the lowest visual sensitivity and the lowest cone density (53%) of the three locations imaged (i.e., 4° temporal-7° superior retina). The scan through 4° superior retina showed marked thinning of NFL on the temporal aspect of the fovea and it gradually became thicker as it approached the optic nerve head.

Figures 3a and 3b show AO-FDOCT images taken at two of the same retinal locations where the AO-flood en face images were acquired in the right eye, 2° temporal-2° superior retina and 4° nasal-4° superior retina. Lower cone density was found at 2° temporal-2° superior retina (62%) (versus 4° nasal-4° superior retina (79%)). The AO-FDOCT image from 2° temporal-2° superior retina revealed an indistinct junction between the outer segment layer and the RPE (OS/RPE), whereas the OS/RPE was better defined at 4° nasal-4° superior retina (labeled 3 in Fig. 3b), although it is not as continuous as shown in the normal retina in Figure 1c.

Both eyes showed a reduction in cone density at all three retinal locations imaged; however, the extent of dark spaces in the mosaic increased with a decrease in visual sensitivity. The AO-FDOCT images also showed structural changes in the cone photoreceptors, making the outer retinal layers more blurred and indistinct especially the OS/RPE junction, the severity of which also varied inversely with HVF sensitivity (i.e., the lower the visual sensitivity, the greater the disturbance at the OS/RPE). Examination of the AO images of cone photoreceptors and the FDOCT images of the retina showed that there is a relationship between the integrity of the cone photoreceptors and the NFL (i.e., the retinal locations that exhibited structural changes in cone photoreceptors revealed either no or markedly thinned NFL.

Case 2: ONHD/NAION—A 54-year-old man who had had bilateral optic nerve head drusen (ONHD) for the past 36 years was imaged. A detailed clinical case report on this patient is published elsewhere,[39] without the benefit of extensive AO-flood imaging. Briefly, both eyes had a long history of significantly constricted visual fields; therefore, HVF central 10° was used instead of the standard 24° for testing. The cause of the ONHD was thought to be bilateral ischemic optic neuropathy of the optic nerve.

AO-flood en face images of cones were taken at three and four different locations of the retina in the right and left eyes, respectively. Figure 4 shows the visual field measurement (central 10–2) with the in vivo images of photoreceptors from 4° nasal-4°inferior retina, 2° superior retina, 4° temporal-4° inferior retina, and 8° temporal-8° inferior retina in the left eye. The cone density was close to being normal at the locations where visual sensitivity was not altered (i.e., 4° nasal-4° inferior retina and 2° superior retina) and then decreased to 57% to 62% of normal at the areas affected by the disease (i.e., 4° temporal-4° inferior retina and 8° temporal-8° inferior retina). The same trend was found in the right eye. The AO-flood en face images were taken at 2° nasal-2° superior retina, 4° temporal-4° inferior retina, and 6° temporal-6° superior retina in the right eye. Cones at 2° nasal-2° superior retina were densely packed, whereas those at 4° temporal-4° inferior retina and 6° temporal-6° superior retina showed evidence of dark spaces in the mosaic. The cone density was close to normal at the center (87%) and then it decreased to 56% of normal in the peripheral locations where visual sensitivity was reduced. Both eyes showed similar cone density measurements for similar visual sensitivity. Some examples of these dark spaces in the cone mosaic are denoted by arrows in Figure 4.

Supplementary Figure S2a shows the FDOCT images taken from the corresponding vertical locations in the right eye. The B-scan images revealed no NFL at 6° superior and 4° inferior to the fovea, and the 2° superior retinal scan showed considerably thinned NFL on the nasal side of the fovea and no NFL at the central and temporal locations. The photoreceptor layers (mostly OS/RPE junction) appeared mottled and blurred, especially at 6° superior and 4° inferior to the fovea. Supplementary Figure S2b shows the FDOCT images taken at the

corresponding vertical locations in the left eye. In general, the central and nasal parts of the retina showed relatively thinned NFL, whereas the temporal retina showed almost no NFL. The photoreceptor layers (mostly at the OS/RPE junction) were somewhat mottled, and some dark blotches were evident on the B-scans at the most peripheral location. This result correlated with the cone density measurements from the AO-flood en face images taken at the locations where the B-scans were acquired.

AO-FDOCT images obtained at the same four retinal locations in the left eye are shown in Figure 5. All four layers (1, 2, 3, and RPE) were visible at all retinal locations except 8° temporal-8° inferior retina, although the OS/RPE was not as well organized at 4° temporal-4° inferior retina. At 8° temporal-8° inferior retina, the OS/RPE was indistinguishable and mottled, which implies structural changes in the outer segments of cone photoreceptors.

Both eyes showed the same trend of results. At the retinal locations where visual sensitivity was reduced, the cone photoreceptors became less reflective; hence dark spaces appeared in the AO-flood en face images (i.e., a reduced number of visible cones) and the OS/RPE junction became blurred and mottled in the AO-FDOCT images. Also, from the FDOCT images, the overlying NFL was either thinned or nonexistent, and the photoreceptor layers appeared blurred at the corresponding locations.

Case 3: SLE/MS—A 45-year-old woman with MS with bilateral optic atrophy and combined SLE and arthritis was tested. The optic atrophy was more severe in the right eye than in the left eye.

Figure 6 shows AO-flood en face images of cone photoreceptors taken from five retinal locations in the right (Fig. 6a) and left (Fig. 6b) eyes, respectively. Note that the visual field test was SITA Standard 24–2 HVF. These in vivo images revealed substantial dark spaces in the cone mosaic at these locations, with the cone density measurement ranging from 3% to 27% of expected normal values[36] in the right eye and from 27% to 52% in the left eye. Some examples of these dark spaces are denoted by arrows in the figure. The cone density in the left eye was much lower than expected for a given visual field result. This is a unique case, among the patients presented here, in that the extent of disturbance in cone photoreceptors was far greater than suggested by sensitivity measured with the HVF. When there was a reduction in visual sensitivity, the cone density was even more reduced from the baseline values than was typical of other subjects. The reason for this finding is not clear. One of the possible reasons is that we were looking at a compounding effect from the systemic and ophthalmic conditions, in this case, SLE and MS.

Supplementary Figures S3a and S3b show FDOCT images obtained at the corresponding retinal locations in both eyes. The right eye had a much thinner NFL than the left at all five locations, and the photoreceptor layer (especially the OS/RPE junction) was not as well defined in both eyes as in normal, as shown in Figure 1b.

AO-FDOCT images were acquired at two of the corresponding retinal locations in the right eye: one with the lowest and one with the highest cone density measurement. Figure 7a shows the AO-FDOCT image from 2° nasal-2°inferior retina (cone density of 3%). All the layers were less distinct and blurred. The OS/RPE junction was not visible, and there were distinct gaps in the IS/OS junction (2 in the figure). The IS/OS junction was better defined at 4° temporal-4° superior retina (cone density of 27%), but the OS/RPE layer was still not visible, implying structural changes in the outer segments of the photoreceptors (Fig. 7b).

Case 4: IIH—A 47-year-old woman with bilateral optic nerve pallor from IIH (pseudotumor cerebri) was tested. The left (worse) eye was chosen for study.

Figure 8 shows the AO-flood en face images of cone photoreceptors from four retinal locations referenced to her visual field measured by a SITA Standard 24–2 HVF. These images also showed dark spaces in the cone mosaic at the retinal locations where the sensitivity was reduced. Some examples of these dark spaces are denoted by arrows in the figure. The cone density ranged from 35% to 92% of normal value and varied with visual sensitivity.

Supplementary Figure S4 shows the FDOCT images acquired at the corresponding locations vertical to the fovea. The B-scan images showed significantly thinned NFL at 2° nasal-7° inferior retina and 4° temporal-4° inferior retina, where the cone density was reduced to 35% and 59%, respectively. At 2° nasal-2° inferior retina (cone density of 81%) and 4° nasal-4° superior retina (cone density of 92%), the NFL was evident, and it was much thicker at 4° nasal-4° superior retina.

Case 5: MS-1—A 43-year-old woman with MS and bilateral optic neuritis tested with SITA standard 24–2 HVF had a normal field in the right eye and a slight defect in the left eye. The extent of optic nerve pallor was slight in both eyes, and the visual acuity was 20/40–2 in each eye. The eye with visual field defect (left eye) was chosen for study.

Figure 9 shows the AO-flood en face images of cone photoreceptors taken at four retinal locations. The inferior retina had reduced visual sensitivity compared with those at superior retina, but the cone density measurements were found to be normal at all four locations. The AO images looked normal with densely packed cones at all locations, as shown in Figure 1a.

Supplementary Figure S5 shows FDOCT images from the corresponding four vertical locations from the fovea, and all the scans appeared normal except for the 7° inferior retina scan where small disruptions were noted at the OS/RPE junction.

AO-FDOCT images also appeared normal, with four distinct layers (1, 2, 3 and RPE) at all locations except at 7° inferior retina where the OS/RPE junction was slightly less distinct (Fig. 10).

There was a slight reduction in visual sensitivity at two of the four locations (3° and 7° inferior retina). However, at 3° inferior retina, all three imaging systems showed normal inner and outer retinal layers, and at 7° inferior retina, a small disruption was detected at the OS/RPE junction by both OCT systems, which may explain the slight reduction in HVF testing.

It was found later that this patient showed fluctuating visual field abnormalities over time, consistent with existing optic neuropathy. When the patient returned for a follow-up examination 3 months later, the visual field had improved to normal. The later normal visual field (Supplementary Fig. S6) can be found online at http://www.iovs.org/cgi/content/full/49/5/2103/DC1.

Case 6: MS-2—Another patient with MS with fluctuating visual field defect was tested: a 34-year-old woman with minor optic disc pallor in both eyes. On the day of imaging, the visual field changes (using SITA standard 24–2 HVF) were similar in both eyes but slightly worse in the left eye; therefore, the left eye was chosen for imaging. Visual acuity was 20/20 in both eyes.

The AO-flood images of cone photoreceptors from four central locations are shown in Figure 11, along with the visual field results and the cone density measurement. The HVF test showed a reduction in visual sensitivity at the inferior nasal part of the visual field. However, the AO-flood images of cone photoreceptors obtained at all four quadrants of the visual field were normal with normal cone density measurements.

Supplementary Figure S7 shows FDOCT images through 2° superior and 2° inferior to the fovea. All the retinal layers appeared normal throughout the whole scan at these two vertical eccentricities.

There was no evidence of retinal changes in this patient. The visual field defects noted earlier in Figure 11 were found to be temporary and returned to normal 8 months later. The later "normal" visual field (Supplementary Fig. S8) can be found online at http://www.iovs.org/cgi/content/full/49/5/2103/DC1.

Stiles-Crawford Effect Imaging

In vivo imaging of cone photoreceptors using AO revealed structural changes in cone photoreceptors in patients with different types of optic neuropathy. The consistent finding in all patients has been that when visual sensitivity is reduced, there is a reduction in cone density related to dark spaces in en face images and an indistinct photoreceptor layer in OCT B-scans. The extent of these changes is related to reductions in visual sensitivity. It is nevertheless possible that these dark spaces contain cones that are rendered invisible by alterations in their waveguide properties.

To address the nature of altered cone photoreceptors in our patients, we modified the angle through which the imaging light was delivered into the eye during AO-flood imaging, to assess the angular tuning characteristics of cone photoreceptors based on the SCE.[29] Roorda and Williams[28] have measured the directionality of cones in healthy retina using AO and showed that the disarray among the cones is small (i.e., when the entrance position of the imaging light was translated, all the cones became blurred collectively). If the dark spaces in the photoreceptor mosaic contain cones that are misaligned from the pupil center, then these cones may be revealed by altering the angle of light delivery into the eye.

The 45-year-old female patient with MS with chronic optic atrophy and lupus (case 3) was selected for SCE imaging at 4° temporal-4° superior retina in the right eye. The results from the central three entrance positions (–1 mm, center, +1 mm in the horizontal meridian) are shown in Figures 12a–c. The image that was taken with central illumination is considered to be the reference image against which all other images taken with eccentric illumination are compared. The cone density at this retinal location was only 27% of the normal value. The SCE imaging was able to bring out some cones that could not be seen under conventional imaging conditions, as shown with green dots. Note that at the same time, some of the cones that were visible with central illumination became less visible when the illumination angle was changed, which is expected from the SCE. Combining all the cones at the various entrance pupil positions still resulted in cone density substantially below that expected in a healthy eye (31% of normal).

The SCE imaging results further verify that cones may undergo substantial structural changes that compromise their integrity at the retinal locations of reduced visual sensitivity. This inference about structural change is consistent with reports of histologic studies.[40] This imaging technique may be useful in characterizing the identity of the dark spaces in en face images (i.e., empty spaces versus areas of cone disarray).

Inner Retinal Layer Thickness Mapping by Volumetric FDOCT

Figure 13 shows the segmentation results of the three-layer NFL–GCL–IPL complex around the macula in one normal subject and three of the patients. In normal retinas, the NFL and GCL were thick enough to be reliably segmented as individual layers, especially around the optic nerve head and at the nasal side of the fovea. However, in the optic neuropathies, either the

NFL or GCL or both were very thin or even absent, making segmentation more difficult; hence, the IPL was included in the thickness maps.

En face thickness maps of the three-layer complex revealed significant thinning of layers in ONHD/NAION (case 2) and IIH (case 4) patients but no change in patient MS1. The thickness maps of the normal subject and patient MS1 were similar, with the thickness ranging between 50 and 110 μm. Both ONHD/ NAION and IIH patients showed marked constriction of visual fields, with slight sparing in the nasal retina, whereas the patient MS1 showed a borderline normal field with some scattered missed spots in the periphery. The thickness of the three-layer complex in the ONHD/NAION and IIH patients mostly ranged between 0 and 50 μm, with a small patch of 75 μm in the IIH patient. The pattern of thickness distribution matched closely the visual field results around the macula in all patients, showing reduced thickness at the locations where visual sensitivity is reduced, and the thickness increased with visual sensitivity. The corresponding visual field maps for ONHD/NAION, IIH, and MS1 are shown in Figure 4, Figure 8, and Figure 9, respectively. This finding, in turn, implies a positive relation between the integrity of cone photoreceptors and the thickness of the three-layer complex.

DISCUSSION

Patients with various types of optic neuropathy including ischemic, inflammatory, and pseudotumor cerebri were imaged with high-resolution imaging systems to assess their retinas at a cellular level in vivo. One en face flood–illumination imaging system equipped with AO (AO-flood–illuminated fundus camera) and two FDOCT systems, one of them equipped with AO (AO-FDOCT) have been used for this study. Each system has unique strengths: the AO-flood–illuminated fundus camera is optimized to produce clear images of the cone mosaic, whereas FDOCT systems allow clear imaging of the entire retinal thickness and sectioning of individual retinal layers in three dimensions, from which thickness maps can be created. AO-FDOCT has the added advantage of sufficient transverse resolution for visualization of individual cellular structures, such as the junction between inner and outer segments of cones and gaps between adjacent cones. Combining all these attributes from each system made it possible to examine cellular structures in three dimensions in living eyes of patients.

A limitation of this study is the small number of subjects. This deficit has to be considered when reviewing the results. The results in this article will be used as a foundation to recruit and study more patients from each type of optic neuropathy over time. Also, as we establish a larger normative database for various age groups, in vivo retinal images from normal subjects will be used to achieve a more direct comparison with diseased retinas instead of using histology data.

The pathogenesis of optic neuropathies has been studied extensively, but these studies have typically focused on inner retina. Hayreh[41,42] showed that there are two types of ischemic optic neuropathy: anterior and posterior. The anterior form is caused by interference with the posterior ciliary artery supply to the optic nerve head and retrolaminar part of the optic nerve, which, in turn, results in visual loss and optic disc edema progressing to optic atrophy in a month or two. The posterior form is due to occlusion of nutrient arteries to the posterior part of the optic nerve and eventually atrophy develops, but in the initial stages, the optic disc appears normal despite visual loss. In contrast, Francois[43] showed that ischemic optic neuropathy is caused by an obstruction of the vascular axial system of the juxtabulbar optic nerve and involves a greater part of the optic nerve.

The pathogenesis of optic neuritis is presumed to be inflammation or demyelination of the optic nerve, similar to that seen in MS.[3] Patients with optic neuritis are more likely to develop MS in the future. Systemic and local infectious and inflammatory disorders can also cause optic

neuritis (e.g., adjacent infection of the meninges, sinuses, or orbit may spread to involve the optic nerve).[3]

Although a variety of factors are implicated as potential causes of pseudotumor cerebri, most cases reveal no clearly identifiable underlying cause.[44] The syndrome of pseudotumor cerebri presents with symptoms and signs of elevated intracranial pressure without additional neurologic abnormality. Common visual symptoms are optic disc pallor, visual field loss, and thinning of the NFL.

According to Köllner's rule, optic nerve diseases usually result in red-green color defects, whereas those diseases that affect the outer retina cause blue-yellow defects. However, patients with glaucoma mostly show the blue-yellow color defect.[45–49] This fact suggests that the color vision defect in glaucoma is more consistent with a retinal degeneration process than one involving only the optic nerve. Schneck and Haegerstrom-Portnoy[18] and Menage et al.[19] reported that patients with optic neuritis show mixed blue-yellow and red-green color defects, instead of the expected red-green defects. This observation further supports the implication of inner and outer retinal involvement in optic neuropathies.

To our knowledge, scant attention has been paid to the integrity of photoreceptors in optic neuropathies. It would be surprising if sustained prolonged visual field loss were accom panied by changes restricted to the nerve fiber layer and ganglion cells without affecting other retinal layers, including photoreceptors. All the patients we tested exhibited a strong association between structural changes in cone photoreceptors and loss of visual sensitivity as well as thinning of the three-layer inner retinal complex. The overall map of inner retinal layer thickness (composed of the NFL, GCL, and IPL) matched the visual field results closely, showing thinning at the locations where visual sensitivity was reduced.

In healthy retina, cones are generally densely packed with a common angular tuning toward the pupil center; hence, under normal imaging conditions (i.e., imaging light entering the pupil through its center) all the cones are detected and produce a regular cone mosaic. However, if cones undergo structural changes due to disease, (1) they may become less reflective as the refractive index difference between inner and outer segments decreases, (2) the direction of angular tuning may change due to less structural support around the cones, and/or (3) they may disappear altogether, leaving behind empty spaces. All these changes may contribute to dark spaces in the en face AO-flood images and indistinct OS/RPE layer in the OCT images. The SCE-imaging technique can be used to address the presence of misaligned cones in these dark spaces by using their waveguide properties. In characterizing the nature of these dark spaces, visual sensitivity is also useful. We have obtained such measures through visual fields and found positive relations with the extent of the dark spaces. Additional tests could include direct stimulation of these dark spaces using AO-guided microperimetry. At this point, we cannot be sure what proportion of the dark spaces in the en face images are made up of misaligned cones or completely dysfunctional cones. Nevertheless, our data demonstrated the validity of SCE imaging in partially characterizing the identity of dark spaces in en face images. In both OCT images, the main structural changes besides thinning of the NFL were detected at the junction of the OS and RPE, whereas the IS/OS was well defined in all cases.

Supplementary Material

Refer to Web version on PubMed Central for supplementary material.

Acknowledgments

The authors thank Bai Xue and Alfred Fuller for assistance in software development.

Supported by National Eye Institute Grant EY014743 and Research to Prevent Blindness (RPB).

References

1. Rodriguez M, Siva A, Cross SA, et al. Optic neuritis: a population-based study in Olmsted County, Minnesota. Neurology 1995;45:244–250. [PubMed: 7854520]
2. Johnson LN, Arnold AC. Incidence of nonarteritic and arteritic anterior ischemic optic neuropathy: population-based study in the state of Missouri and Los Angeles County, California. J Neuroophthalmol 1994;14:38–44. [PubMed: 8032479]
3. Miller, NR.; Newman, NJ.; Biousse, V.; Kerrison, JB. Walsh and Hoyt's Clinical-Neuroophthalmology. Vol. 6th ed.. Philadelphia: Lippincott Williams & Wilkins; 2005.
4. Waxman SG. Membranes, myelin and the pathophysiology of multiple sclerosis. N Engl J Med 1982;306:1529–1533. [PubMed: 7043271]
5. Steel DH, Waldock A. Measurement of the retinal nerve fiber layer with scanning laser polarimetry in patients with previous demyelinating optic neuritis. J Neurol Neurosurg Psychiatry 1998;64:505–509. [PubMed: 9576544]
6. Roh S, Noecker RJ, Schuman JS, Hedges TR 3rd, Weiter JJ, Mattox C. Effect of optic nerve head drusen on nerve fiber layer thickness. Ophthalmology 1998;105:878–885. [PubMed: 9593392]
7. Katz BJ, Pomeranz HD. Visual field defects and retinal nerve fiber layer defects in eyes with buried optic nerve drusen. Am J Ophthalmol 2006;141:248–253. [PubMed: 16458676]
8. Bianchi-Marzoli S, Rizzo JF 3rd, Brancato R, Lessell S. Quantitative analysis of optic disc cupping in compressive optic neuropathy. Ophthalmology 1995;102(3):436–440. [PubMed: 7891982]
9. Monteiro MLR, Leal BC, Rosa AAM, Bronstein MD. Optical coherence tomography analysis of axonal loss in band atrophy of the optic nerve. Br J Ophthalmol 2004;88:896–899. [PubMed: 15205233]
10. Sanders EA, Volkers AC, Van der Poel JC, et al. Spatial contrast sensitivity function in optic neuritis. Neuroophthalmoly 1984;4:255–259.
11. Optic Neuritis Study Group. The clinical profile of acute optic neuritis: experience of the optic neuritis treatment trial. Arch Ophthalmol 1991;109:1673–1678. [PubMed: 1841573]
12. Rosen JA. Pseudoisochromatic visual testing in the diagnosis of disseminated sclerosis. Trans Am Neurol Assoc 1965;90:283–284. [PubMed: 5857763]
13. Marre, M. The investigation of acquired color deficiencies. Presented at the Second Congress of the International Color Association, New York University; July 2–6, 1973; London. Adam Hilger Publishers; 1973.
14. Trusiewicz D. Farnsworth 100 hue test in diagnosis of ethambutol-induced damage to the optic nerve. Ophthalmology 1975;171:425–431.
15. Griffin JF, Wray SH. Acquired color vision defects in retrobulbar neuritis. Am J Ophthalmol 1978;86:193–201. [PubMed: 686121]
16. Wybar KC. The ocular manifestations of disseminated sclerosis. Proc Roy Soc Med 1952;45:315–319. [PubMed: 14941838]
17. Lynn BH. Retrobulbar neuritis: a survey of the present condition of cases occurring over the last fifty-six years. Trans Ophthalmol Soc UK 1959;79:701–716. [PubMed: 14419158]
18. Schneck ME, Haegerstrom-Portnoy G. Color vision defect type and spatial vision in the optic neuritis treatment trial. Invest Ophthalmol Vis Sci 1997;38:2278–2289. [PubMed: 9344351]
19. Menage MJ, Papakostopoulos D, Hart JCD, et al. The Farnsworth-Munsell 100 hue test in the first episode of demyelinating optic neuritis. Br J Ophthalmol 1993;77:68–74. [PubMed: 8435421]
20. Boghen DR, Glaser JS. Ischemic optic neuropathy: the clinical profile and natural history. Brain 1975;98:689–708. [PubMed: 1218373]
21. Repka MX, Savino PJ, Schatz NJ, Sergott RC. Clinical profile and long-term implications of anterior ischemic optic neuropathy. Am J Ophthalmol 1983;96:478–483. [PubMed: 6624829]
22. Orcutt JC, Page NGR, Sanders MD. Factors affecting visual loss in benign intracranial hypertension. Ophthalmology 1984;91:1303–1312. [PubMed: 6514295]
23. Vaegan, Graham SL, Goldberg I, Buckland L, Hollows FC. Flash and pattern electroretinogram changes in optic atrophy and glaucoma. Exp Eye Res 1995;60:697–706. [PubMed: 7641852]

24. Panda S, Jonas JB. Decreased photoreceptor count in human eyes with secondary angular-closure glaucoma. Invest Ophthalmol Vis Sci 1992;33(8):2532–2536. [PubMed: 1634350]
25. Nork TM, Ver Hoeve JN, Poulsen GL, et al. Swelling and loss of photoreceptors in chronic human and experimental glaucomas. Arch Ophthalmology 2000;118:235–245.
26. Werner JS, Choi SS, Zawadzki RJ. High-resolution imaging of retinal and optic nerve head changes in optic neuropathies. International Perimetric Society. Acta Ophthalmol Scand 2006;84(4):587.
27. Choi SS, Doble N, Hardy JL, et al. In-vivo imaging of the photoreceptor mosaic in retinal dystrophies and correlations with retinal function. Invest Ophthalmol Vis Sci 2006;47:2080–2092. [PubMed: 16639019]
28. Roorda A, Williams DR. Optical fiber properties of individual human cones. J Vision 2002;2:404–412.
29. Enoch, JM.; Tobey, FL. Vertebrate Photoreceptor Optics: Springer Series in Optics Sciences. Vol. 23. Heidelberg, Germany: Springer; 1981.
30. Zawadzki R, Jones S, Olivier S, et al. Adaptive-optics optical coherence tomography for high-resolution and high-speed 3D retinal in vivo imaging. Opt Express 2005;13:8532–8546. [PubMed: 19096728]
31. Alam S, Zawadzki RJ, Choi SS, et al. Clinical application of rapid serial Fourier-domain optical coherence tomography for macular imaging. Ophthalmology 2006;113:1425–1431. [PubMed: 16766031]
32. Zawadzki RJ, Fuller AR, Wiley DF, Hamann B, Choi SS, Werner JS. Support vector machine-based algorithm for segregation of retinal structures in volumetric optical coherence tomography data sets. J Biomed Opt 2007;12:041206. [PubMed: 17867795]
33. Theévenaz P, Ruttimann UE, Unser M. A pyramid approach to subpixel registration based on intensity. IEEE Trans Image Process 1998;7:27–41. [PubMed: 18267377]
34. Zawadzki RJ, Choi SS, Jones SM, Olivier SS, Werner JS. Adaptive optics-optical coherence tomography: optimizing visualization of retinal structures in three dimensions. J Opt Soc Am A 2007;24:1373–1383.
35. Xue B, Choi SS, Doble N, Werner JS. Photoreceptor counting and image montaging of en face retinal images from an adaptive optics fundus camera. J Opt Soc Am A 2007;24(5):1364–1372.
36. Curcio CA, Sloan KR, Kalina RE, Hendrickson AE. Human photoreceptor topography. J Comp Neurol 1990;292:497–523. [PubMed: 2324310]
37. Wolfing J, Chung M, Carroll J, Roorda A, Williams DR. High resolution retinal imaging of cone rod dystrophy. Ophthalmology 2006;113(6):1014–1019.
38. Li KY, Roorda A. Automated identification of cone photoreceptors in adaptive optics retinal images. J Opt Soc Am A 2007;24(5):1358–1363.
39. Choi SS, Zawadzki RJ, Greiner MA, Werner JS, Keltner JL. High-resolution retinal imaging of optic nerve head drusen showing nerve fiber layer loss and photoreceptor changes. J Neuroophthalmol. In press
40. Sipperley MJO, Quigley HA, Gass DM. Traumatic retinopathy in primates, the explanation of commotio retinae. Arch Ophthalmol 1978;96:2267–2273. [PubMed: 718521]
41. Hayreh SS. Pathogenesis of cupping of the optic disc. Br J Ophthalmol 1974;58(10):863–876. [PubMed: 4375487]
42. Hayreh SS. Blood supply of the optic nerve head and its role in optic atrophy, glaucoma and edema of the optic disc. Br J Ophthalmol 1969;53(11):721–748. [PubMed: 4982590]
43. Francois J. Vascular pseudopapillitis: ischemic optic neuropathy. Ann Ophthalmol 1976;8(8):901–919. [PubMed: 962265]
44. Friedman DI. Pseudotumour cerebri. Neurosurg Clin North Am 1999;10(4):609–621.
45. Pokorny J, Smith VC. Eye disease and color defects. Vis Res 1986;26:1573–1584. [PubMed: 3303675]
46. Grutzner P, Schleicher S. Acquired color vision defects in glaucoma patients. Mod Probl Ophthalmol 1972;11:136–140. [PubMed: 4544950]
47. Fishman GA, Krill AE, Fishman M. Acquired color vision defects in patients with open-angle glaucoma and ocular hypertension. Mod Probl Ophthalmol 1974;13:335–338. [PubMed: 4548150]

48. Lakowski R, Drance SM. Acquired dyschromatopsias: the earliest functional losses in glaucoma. Doc Ophthalmol Proc Ser 1979;19:159–165.

49. Poinoosawmy D, Nagasubramanian S, Gloster J. Color vision in patients with chronic simple glaucoma and ocular hypertension. Br J Ophthalmol 1980;64:852–857. [PubMed: 7426556]

(a)

21-year-old normal retina

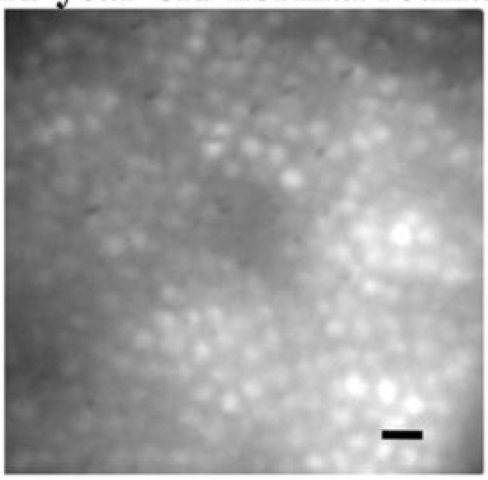

4° Temporal Retina

45-year-old normal retina

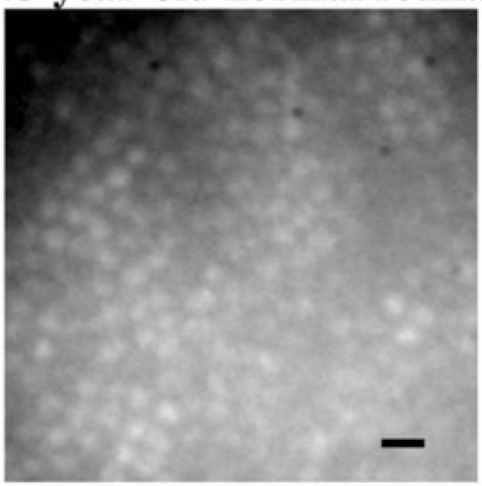

4° Temporal 4° Superior retina

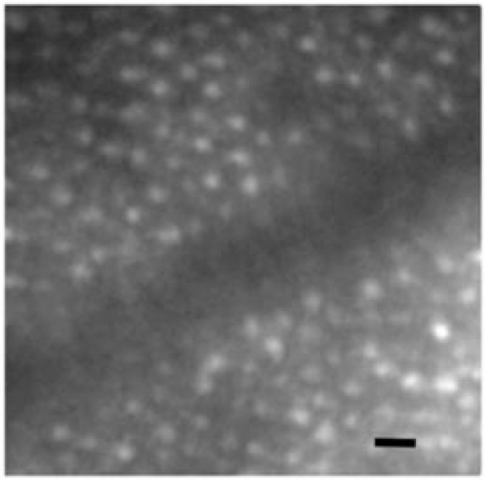

7° Temporal 3° Inferior Retina

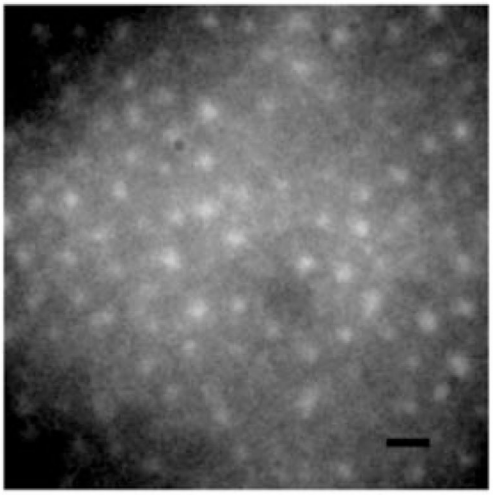

6° Temporal 7° Inferior Retina

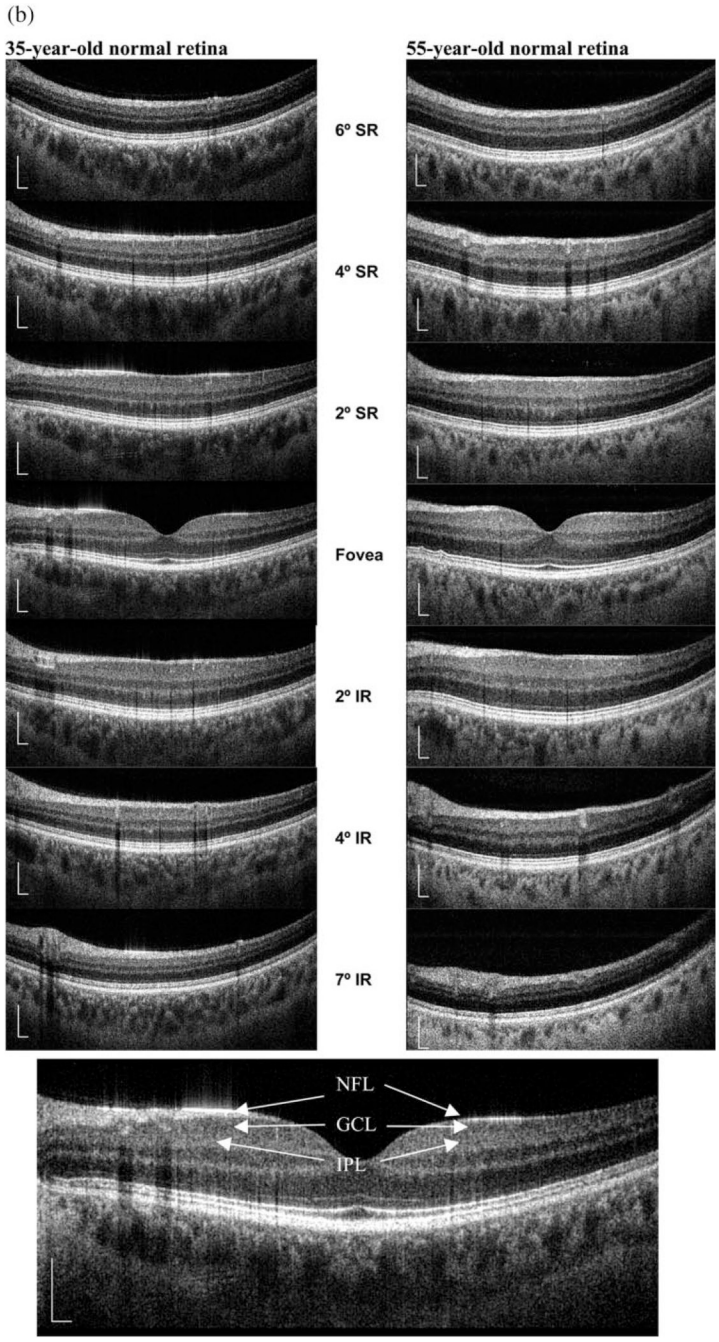

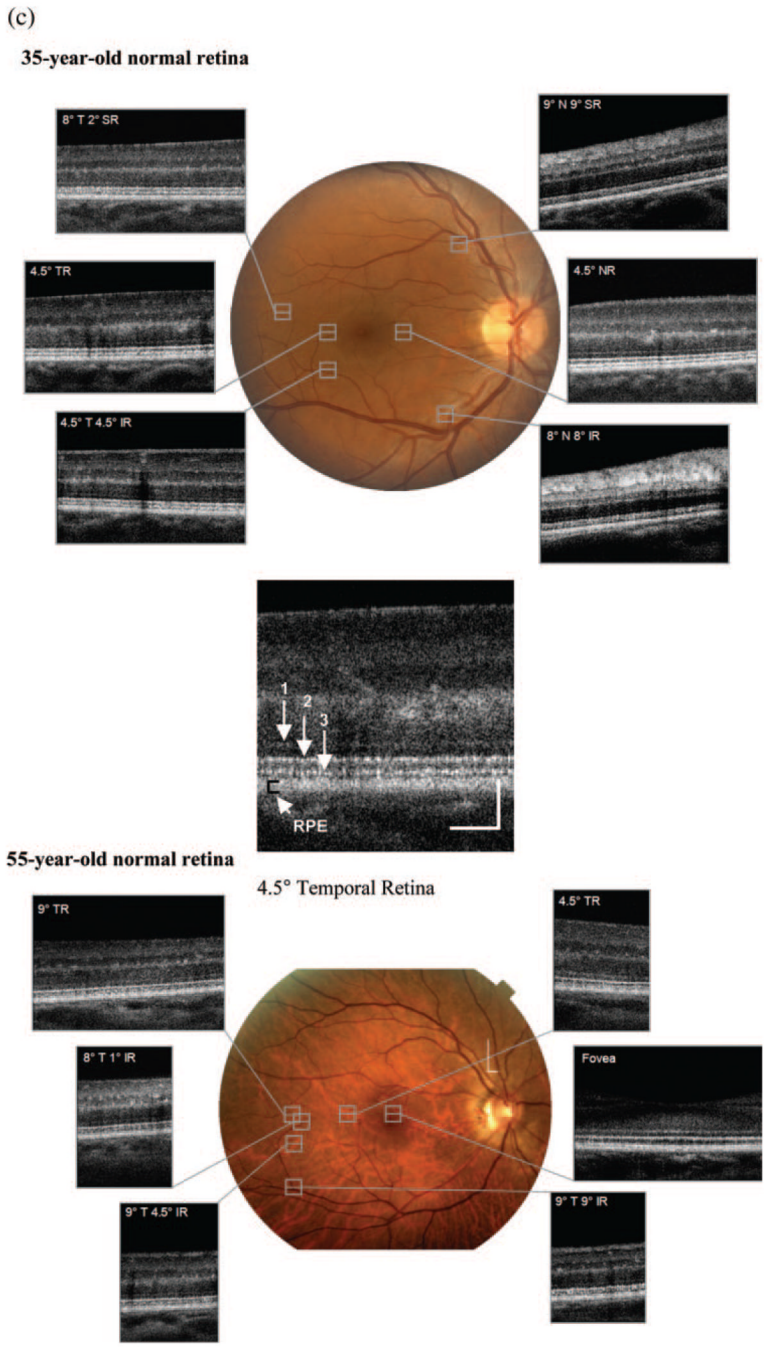

FIGURE 1.

Images of normal retina in young and older subjects. (**a**) An en face image of the photoreceptor mosaic obtained with the AO-flood–illuminated fundus camera at 4° temporal-4° superior retina and 6° temporal-7° inferior retina in a 45-year-old eye and at 4° temporal retina and 7° temporal-3° inferior retina in a 21-year-old eye. Darker areas in the image represent shadows cast by blood vessels from layers above the photoreceptors. Cones were visible in these dark areas, even though they appeared fainter. (**b**) Corresponding FDOCT B-scans through the fovea and six other retinal locations in a 35-year-old and a 55-year-old eye. B-scans were taken at 6° superior retina, 4° superior retina, 2° superior retina, fovea, 2° inferior retina, 4° inferior retina, 7° inferior retina. The NFL is much thicker on the nasal side of the fovea than on the

temporal side. An FDOCT image taken at the fovea of the younger subject is shown for labeling purposes. (**c**) AO-FDOCT images were taken at six different locations in the retina in the same 35- and 55-year-old eyes. These locations are indicated on the fundus picture of the eye. An AO-FDOCT image at 4.5° temporal retina is shown for labeling purposes. 1: ELM, 2: IS/OS, 3: tip of OS of photoreceptors making contact with microvilli of the RPE (OS/RPE), RPE: retinal pigment epithelium; T, temporal; N, nasal; S, superior; I, inferior; R, retina. Scale bar: (**a**) 10 μm; (**b**, **c**) 100 μm.

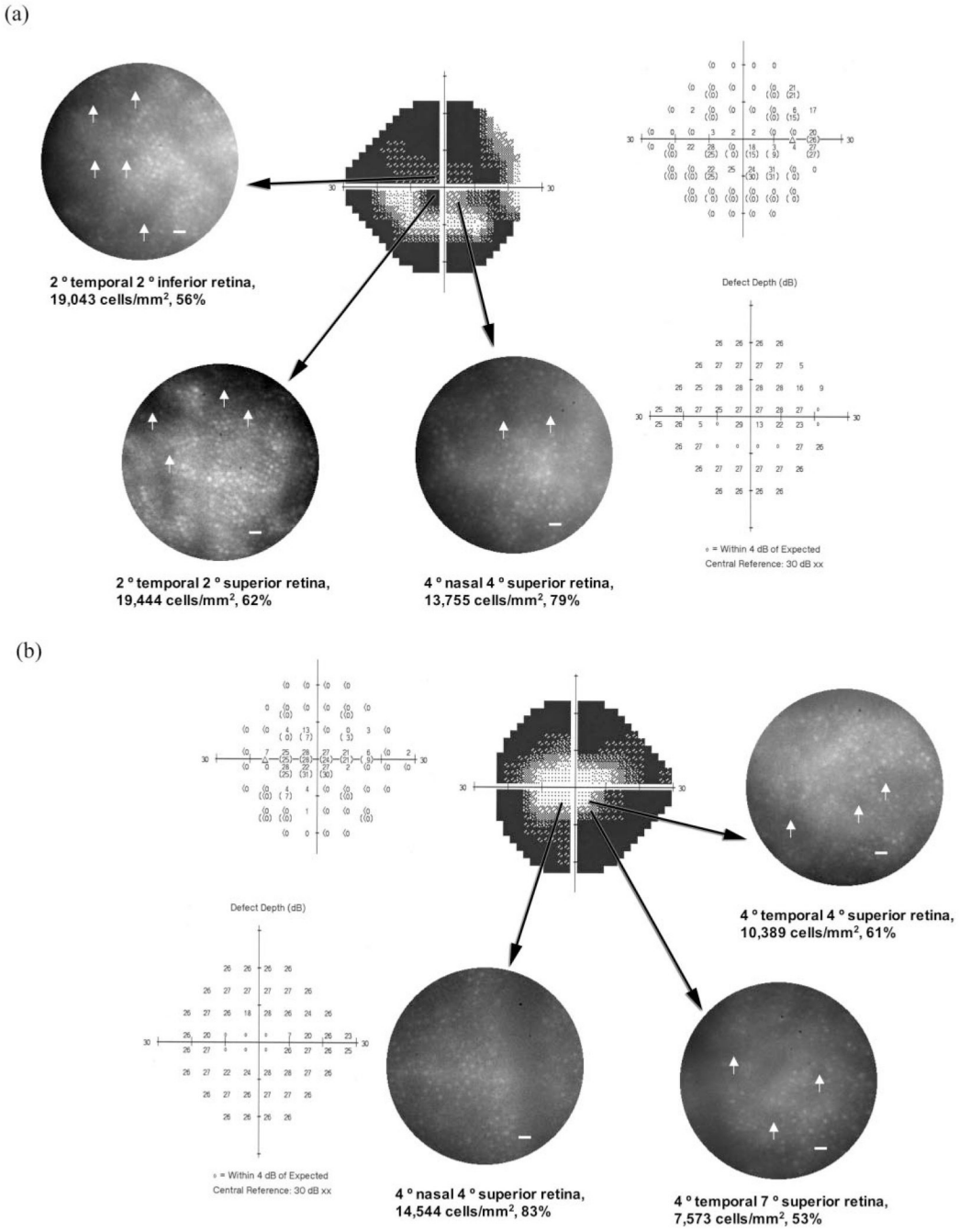

FIGURE 2.

AO-flood en face images of both eyes of the patient with NAION (case 1), taken at three retinal locations: (**a**) right eye and (**b**) left eye. The visual field was tested with FAST Pac Size V 24–2 (Carl Zeiss Meditec, Inc., Dublin, CA). Relative percentages of cone density in relation to the histology of Curcio et al.[36] are also shown in (**a**) and (**b**). *Arrows*: some examples of the dark spaces. Scale bar, 10μm.

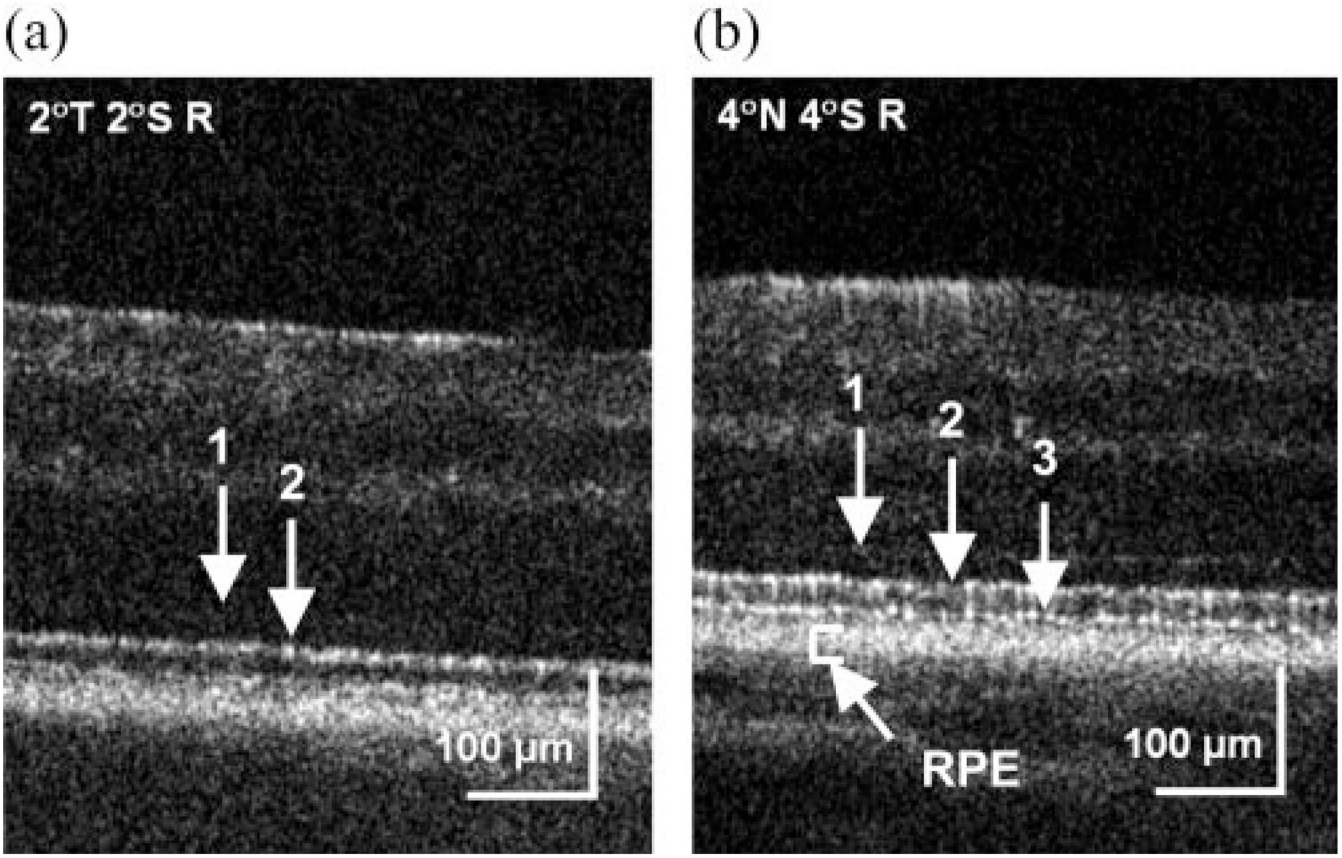

FIGURE 3.
AO-FDOCT images at two retinal locations in the right eye of the patient with NAION (case 1): (**a**) 2° temporal-2° superior retina and (**b**) 4° nasal-4° superior retina. 1: ELM, 2: IS/OS, 3: OS/RPE. T, temporal; N, nasal; S, superior; R, retina.

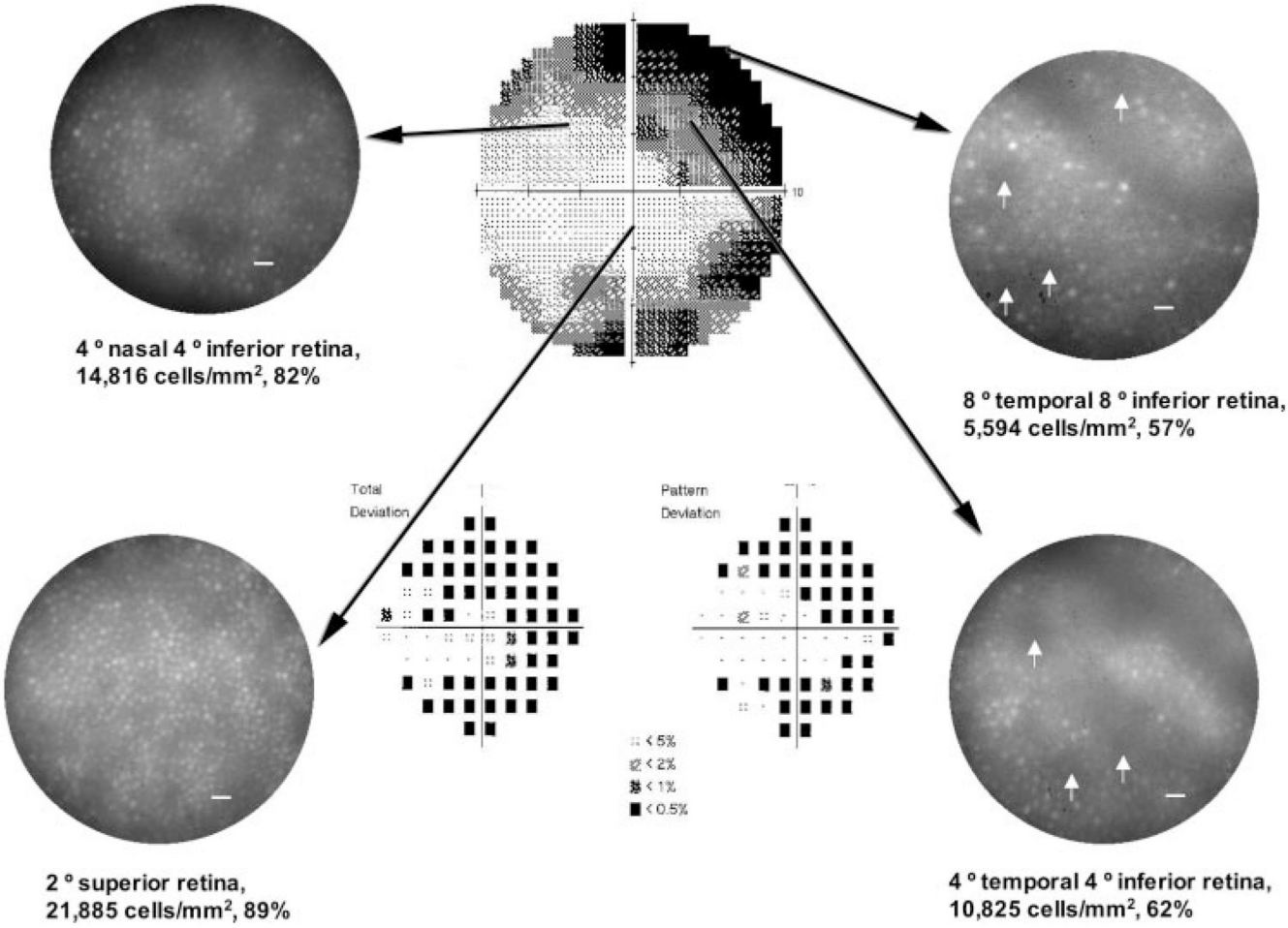

FIGURE 4.

AO-flood en face images of the left eye of the patient with ONHD (case 2), taken at four retinal locations. The visual field is a 10–2 central HVF. Relative percentage of cone density in relation to the histology of Curcio et al.[36] are also shown. *Arrows*: examples of the dark spaces. Scale bar, 10 μm.

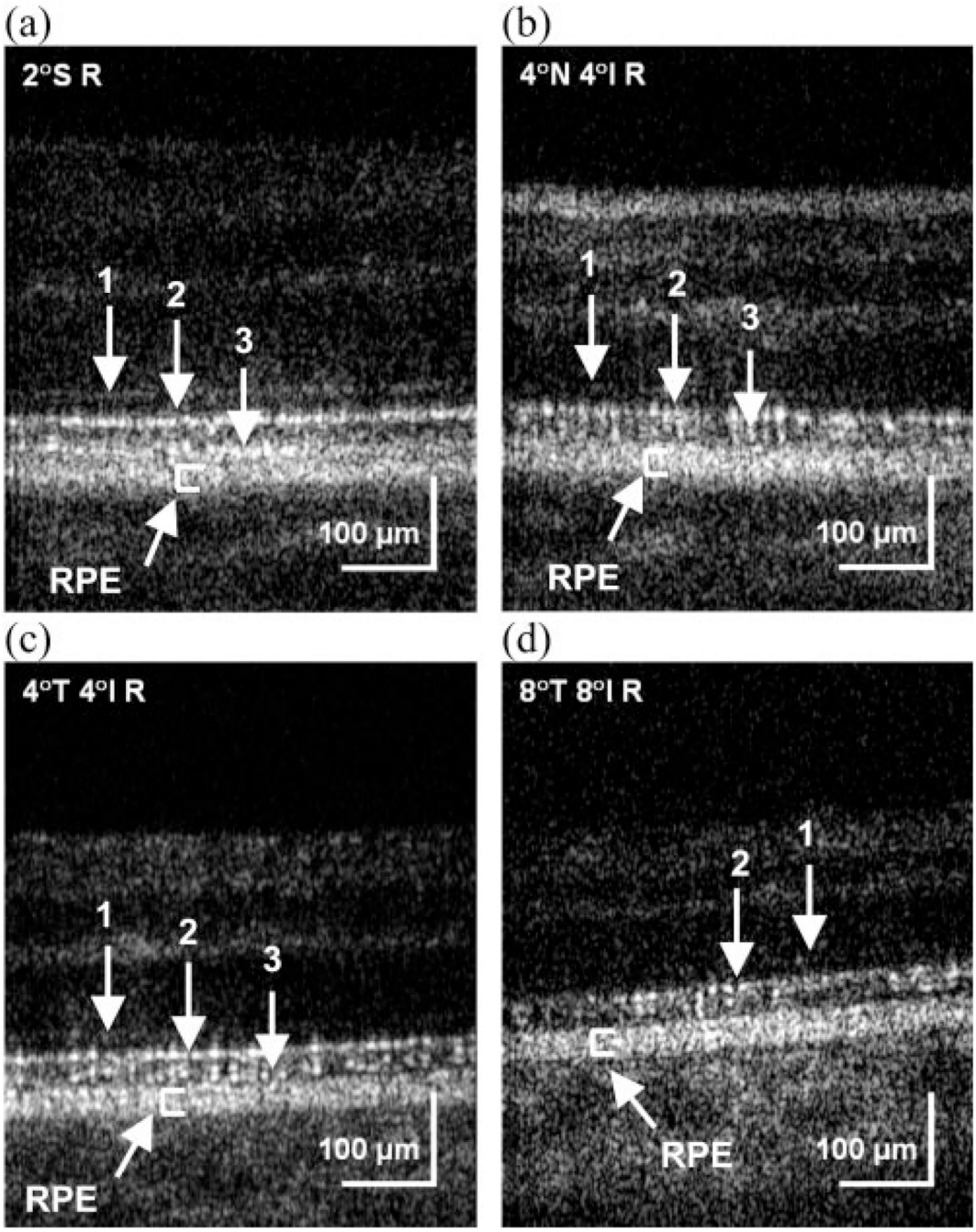

FIGURE 5.

AO-FDOCT images at four retinal locations in the left eye of the patient with ONHD (case 2): (**a**) 2° superior retina, (**b**) 4° nasal-4° inferior retina, (**c**) 4° temporal-4° inferior retina, and (**d**) 8° temporal-8° inferior retina. 1: ELM, 2: IS/OS, 3: OS/RPE. T, temporal; N, nasal; S, superior; I, inferior; R, retina.

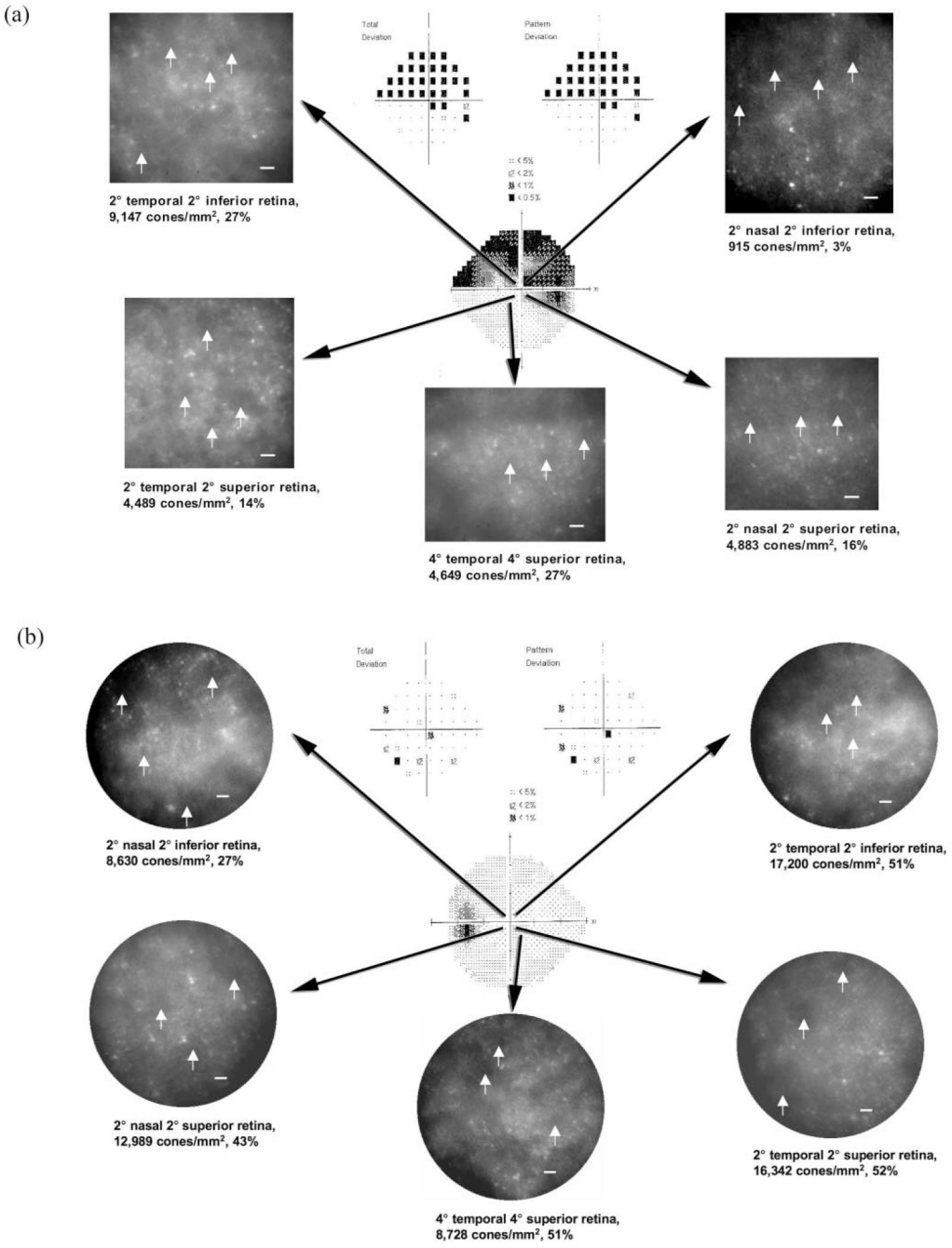

FIGURE 6.

AO-flood en face images of both eyes of the patient with SLE/MS (Case 3) at the same five retinal locations in each eye: (**a**) right eye and (**b**) left eye. The visual field was tested with the SITA Standard 24-2 HVF (Carl Zeiss Meditec, Inc., Dublin, CA). Relative percentage of cone density measurements in relation to the histology of Curcio et al.[36] are also shown. *Arrows*: examples of the dark spaces. Scale bar, 10 μm.

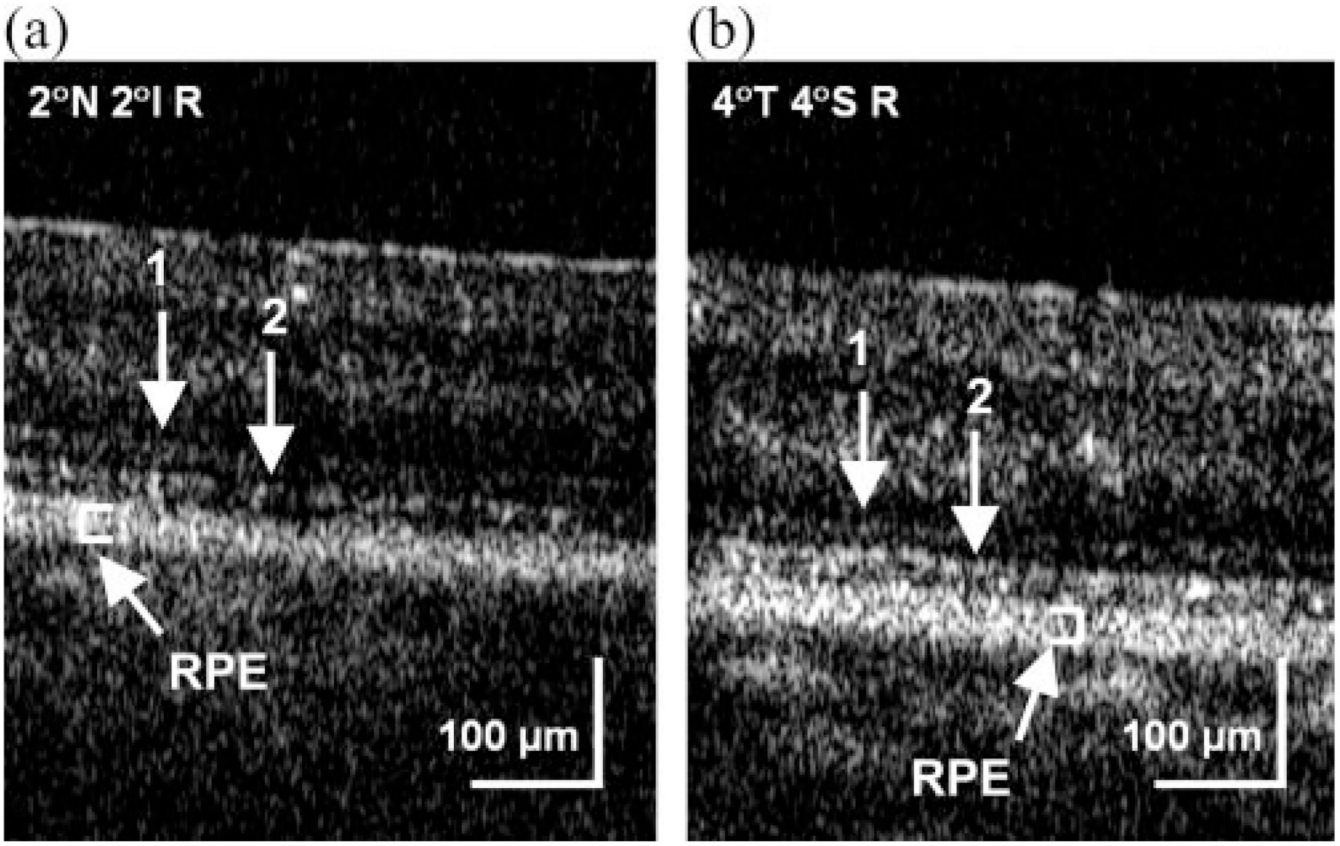

FIGURE 7.

AO-FDOCT images at two retinal locations in the right eye of the patient with SLE/MS (case 3): (**a**) 2° nasal-2° inferior retina and (**b**) 4° temporal-4° superior retina. 1: ELM, 2: IS/OS. T, temporal; N, nasal; S, superior; I, inferior; R, retina.

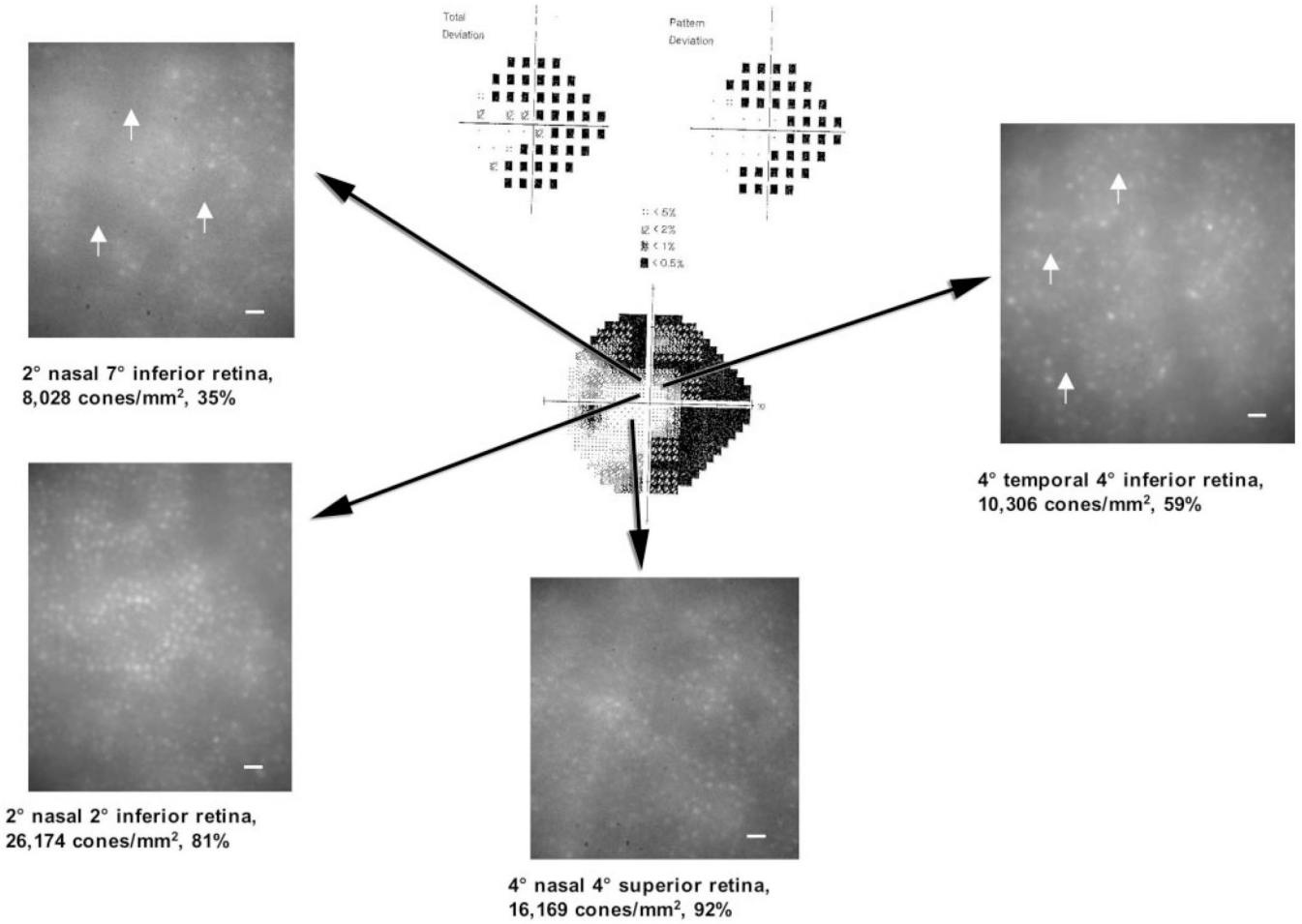

FIGURE 8.

AO-flood en face images taken from the IIH patient (case 4) at four retinal locations in the left eye. The visual field was tested with SITA Standard 24-2 HVF (Carl Zeiss Meditec, Inc., Dublin, CA). Relative percentages of cone density measurements in relation to the histology of Curcio et al.[36] are also shown. *Arrows*: examples of the dark spaces. Scale bar, 10 μm.

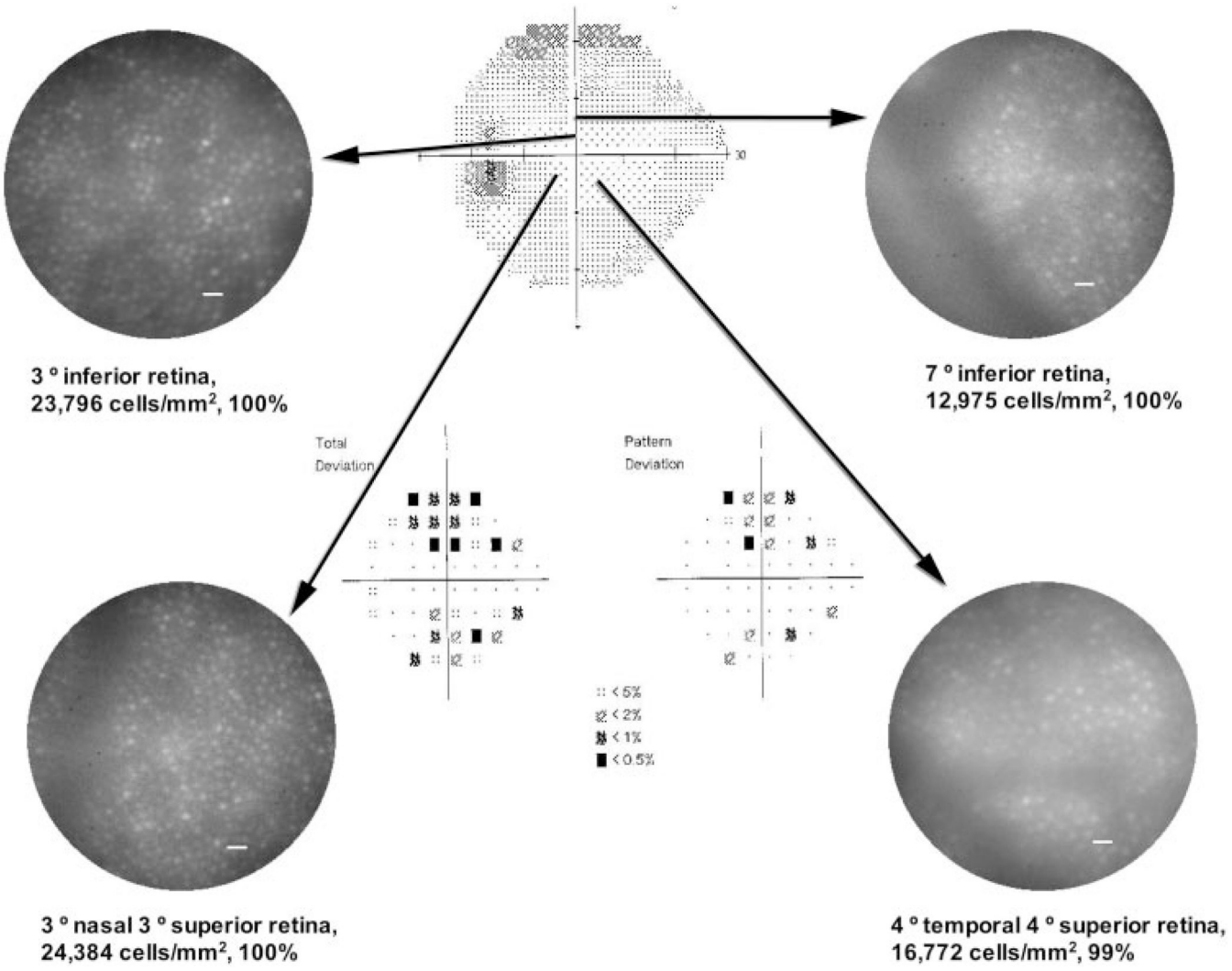

FIGURE 9.

AO-flood en face images taken from patient MS1 (case 5) at four retinal locations in the left eye. Note that the visual field is SITA Standard 24-2 HVF (Carl Zeiss Meditec, Inc., Dublin, CA). Relative percentages of cone density measurements in relation to histology of Curcio et al.[36] are also shown. Scale bar, 10 μm.

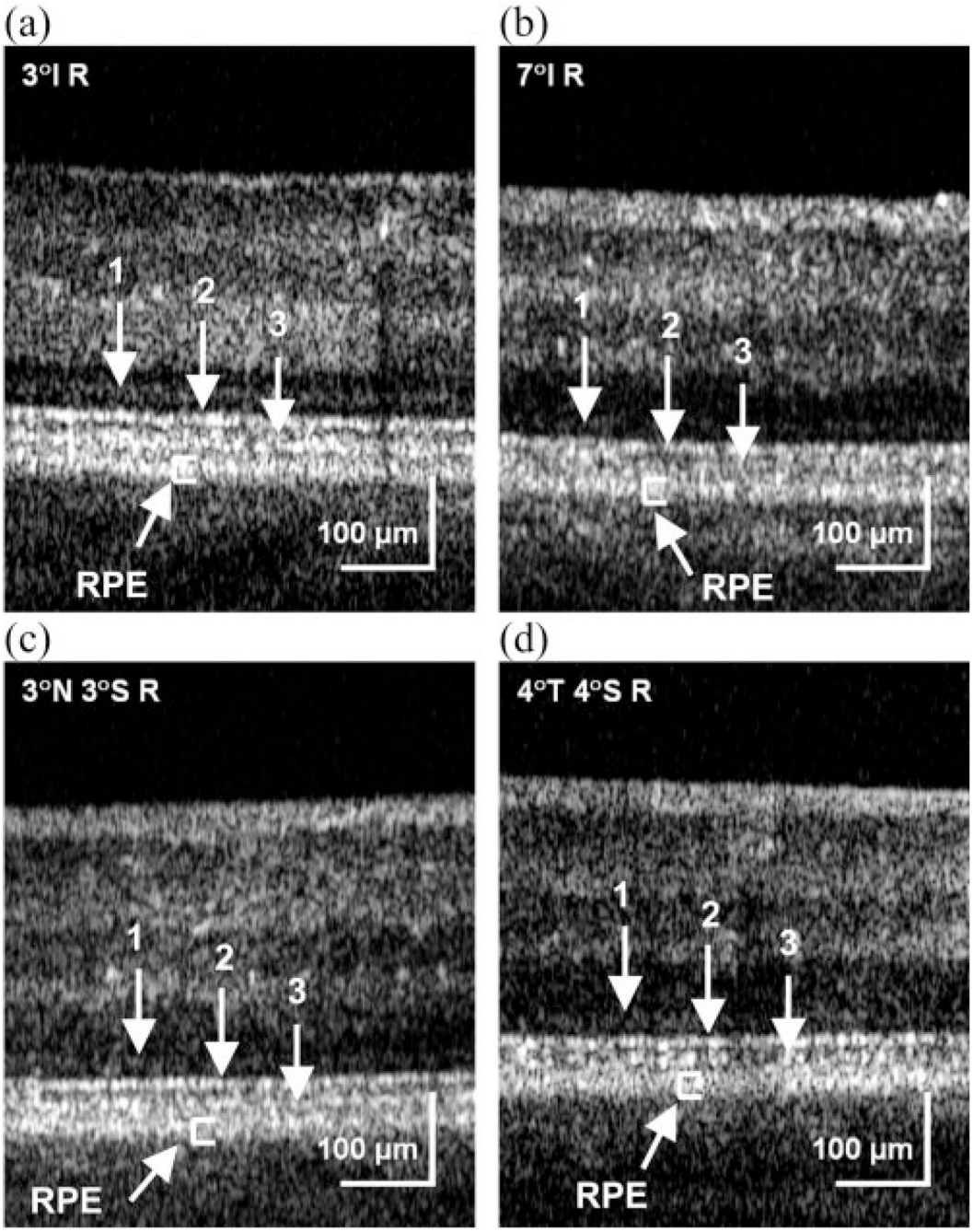

FIGURE 10.
AO-FDOCT images at four retinal locations in the left eye of patient MS1 (case 5): (**a**) 3° inferior retina, (**b**) 7° inferior retina, (**c**) 3° nasal-3° superior retina, and (**d**) 4° temporal-4° superior retina. 1: ELM, 2: IS/OS. T, temporal; N, nasal; S, superior; I, inferior; R, retina.

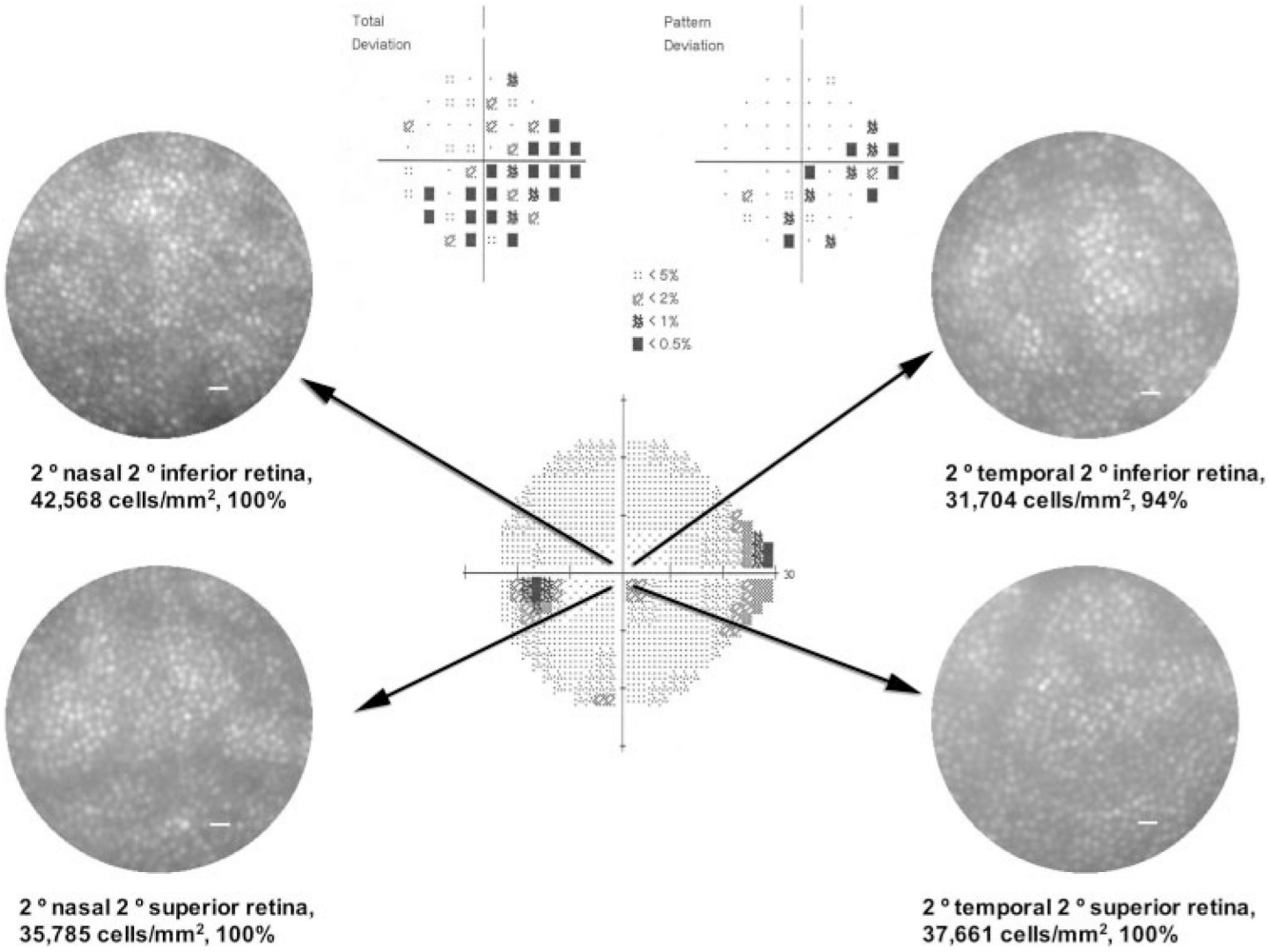

FIGURE 11.

AO-flood en face images taken from patient MS2 (case 6) at four retinal locations in the left eye. The visual field test was SITA Standard 24-2 HVF (Carl Zeiss Meditec, Inc., Dublin, CA). Relative percentages of cone density measurements in relation to the histology of Curcio et al.[36] are also shown. Scale bar, 10 μm.

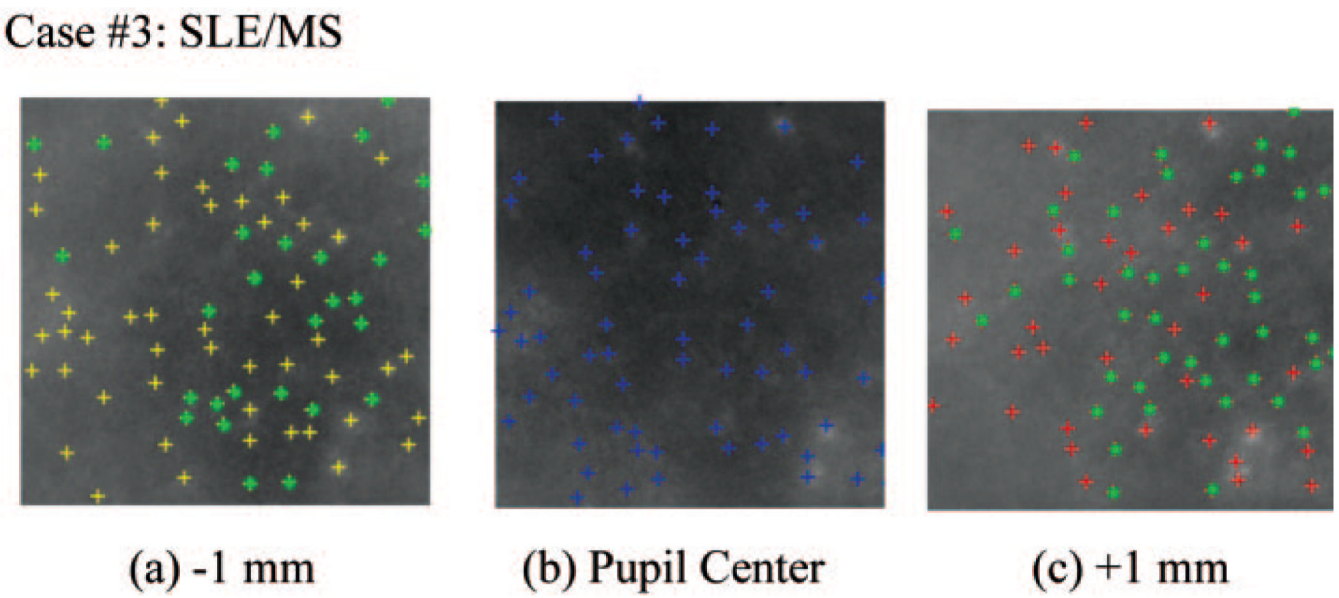

FIGURE 12.

(**a–c**) A cropped image (0.5°) taken at 4° temporal-4° superior retina in the right eye of the patient with SLE/MS (case 3). *Green dots:* the cones that became visible by altering the pupil entrance position of the imaging light. *Crosses:* the cones that are common to each image (*yellow*, −1 mm nasal; *blue*, pupil center; *red*, +1 mm temporal). Images acquired with three different entrance positions of the imaging light (±1 mm from the pupil center and the pupil center) are shown.

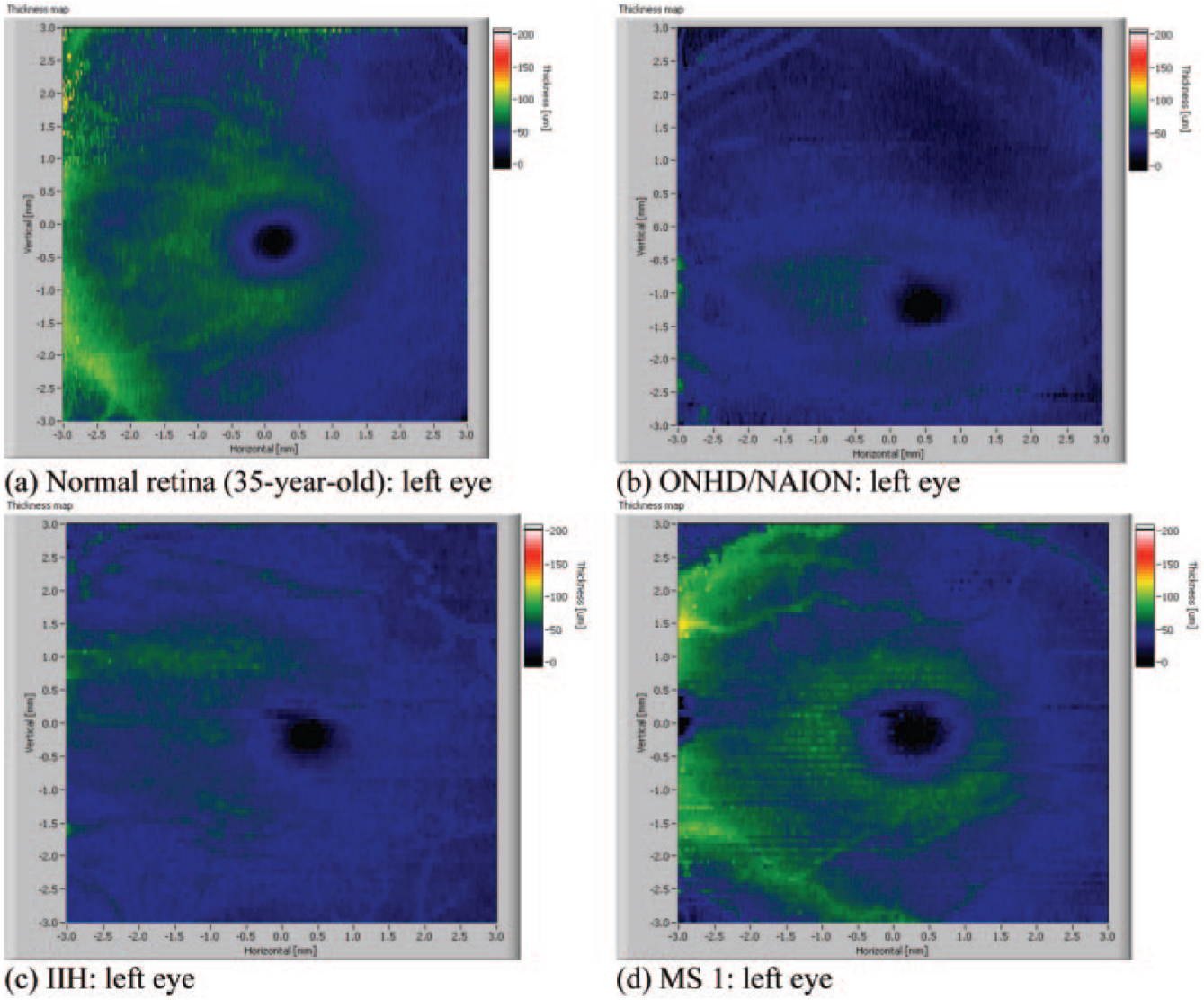

FIGURE 13.

Two-dimensional thickness maps of the three-layer NFL-GCL-IPL complex around the macula from a normal retina (**a**) in a 35-year-old left eye and eyes of three of the patients: (**b**) ONHD/NAION (case 2): left eye, (**c**) IIH (case 4): left eye, (**d**) MS 1 (case 5): left eye.

Table 1
Summary of Clinical Findings

	Right Eye	Left Eye
Case 1: NAION; male; age: 57 years; diagnosis: bilateral NAION		
History	Bilateral NAION, diagnosed in left eye 1994, right eye 1996	
Visual acuity	20/60+2	20/20–2
Color vision	1½/6 AO HRR plates	4/6 AO HRR plates
Visual field	HVF 24–2 FASTPAC, Size V test target, see Fig. 2a	HVF 24–2 FASTPAC, Size V test target, see Fig. 2b
	Severe, marked peripheral constriction and depression with central foveal threshold of 30 dB, with relative sparing of central island of 10–15°	Severe overall constriction and peripheral depression with only a central island, foveal thres hold of 33 dB
IOP (mm Hg)	19	20
Stratus OCT: NFL thickness (μm)	Not available	Not available
Fundus	4+ optic atrophy with narrowing of the blood vessels and posterior vitreous detachment (PVD)	4+ optic atrophy with narrowing of the blood vessels and posterior vitreous detachment (PVD)
Case 2: ONHD/NAION; male; age: 54; diagnosis: optic nerve head drusen and NAION		
History	Optic nerve head drusen and NAION	
Visual acuity	20/15	20/15
Color vision	4/6 AO HRR plates	6/6 AO HRR plates
Visual field	HVF 10–2 FASTPAC, size III test target	HVF 10–2 FASTPAC, size III test target, see Fig. 4
	Severely constricted to 5–8°, MD −18.63 dB, foveal threshold 34 dB	Severely constricted to 5–8°, MD −15.92 dB, foveal threshold 35 dB
IOP (mm Hg)	11	13
Stratus OCT: NFL thickness (μm)	Avg. thickness abnormal 48.99 (overall severe diffuse thinning [1%])	Avg. thickness abnormal 41.23 (overall severe diffuse thinning [11%])
Fundus	4+ optic nerve drusen with almost total loss of the NFL with normal macula and vessels	4+ optic nerve drusen with almost total loss of the NFL with normal macula and vessels
Case 3: SLE/MS; female; age: 45; diagnosis: systemic lupus erythematosus and multiple sclerosis with arthritis		
History	Systemic lupus erythematosus and multiple sclerosis with arthritis	
Visual acuity	20/60	20/20
Color vision	0/6 AO HRR plates	6/6 AO HRR plates
Visual field	HVF 24–2 SITA Std., size III test target, see Fig. 6a	HVF 24–2 SITA Std., size III test target, see Fig. 6b
	Dense superior altitudinal loss, MD −13.49 dB, foveal threshold 22 dB	Scattered missed spots, MD −1.76, foveal threshold 36 dB
IOP (mm Hg)	15	16
Stratus OCT: NFL thickness (μm)	Avg. thickness abnormal 47.41 (Overall severe diffuse thinning [1%])	Avg. thickness abnormal 75.67 (Moderate overall thinning [5%] with thinning superior quadrant [1%] and temporal quadrant [5%])
Fundus	2–3+ optic nerve pallor, normal macula and vessels	2+ optic nerve pallor
Case 4: IIH; female; age: 47; diagnosis: idiopathic intracranial hypertension (pseudotumor cerebri)		
History	Idiopathic intracranial hypertension (Pseudotumor Cerebri) status LP shunt and Arnold-Chiari malformation decompression	
Visual acuity	20/15−	20/20+

	Right Eye	Left Eye
Color vision	6/6 AO HRR plates	6/6 AO HRR plates
Visual field	HVF 24–2 SITA Std., size III test target	HVF 24–2 SITA Std., size III test target, see Fig. 8
	Subtle inferionasal step, MD −0.27 dB, foveal threshold 38 dB	Dense superior and inferior arcuate scotoma, MD −21.84 dB, foveal threshold 37 dB
IOP (mm Hg)	16	16
Stratus OCT: NFL thickness (μm)	Avg. thickness normal 98.12 (focal thinning at 6 o'clock [5%], 10 and 11 o'clock [5%])	Avg. thickness abnormal 49.06 (overall severe diffuse thinning [1%])
Fundus	1–2+ optic nerve pallor, otherwise normal macula and vessels	3+ diffuse optic nerve pallor, normal macula and vessels
Case 5: MS 1; female; age: 43; diagnosis: multiple sclerosis		
History	Optic neuritis in both eyes and Multiple Sclerosis	
Visual acuity	20/40–2	20/40–2
Color vision	5/6 AO HRR plates	5/6 AO HRR plates
Visual field	HVF 24–2 SITA Std., size III test target	HVF 24–2 SITA Std., size III test target, see Fig. 9
	Mild depression with scattered abnormalities but still within normal limits, foveal threshold 35 dB, MD −1.94 dB	Some scattered missed spots in the periphery, borderline field with foveal threshold 35 dB, MD −3.74 dB
IOP (mm Hg)	15	17
Stratus OCT: NFL thickness (μm)	Avg. thickness normal 87.82 (Focal thinning at 5 o'clock [1%])	Avg. thickness normal 85.40 (Temporal thinning [5%])
Fundus	3/10 cup with slight optic nerve pallor	3/10 cup with slight optic nerve pallor
Case 6: MS 2; female; age: 34; diagnosis: multiple sclerosis		
History	Multiple sclerosis	
Visual acuity	20/20	20/20
Color vision	6/6 AO HRR plates	6/6 AO HRR plates
Visual field	HVF 24–2 SITA Std., size III test target	HVF 24–2 SITA Std., size III test target, see Fig. 11
	A very subtle superior partial arcuate field defect with a mild inferior partial arcuate field defect with some moderate loss in the paracentral area, foveal threshold, 35 dB, MD −3.94 dB	Superior partial arcuate field defect with a nasal step and a moderate inferior arcuate field defect, foveal threshold is slightly reduced at 33 dB, MD −5.83 dB
IOP (mm Hg)	16	13
Stratus OCT: NFL thickness (μm)	Avg. thickness normal 96.07 (focal thinning at 8 o'clock [1%], 7 o'clock [5%])	Avg. thickness normal 94.65 (Focal thinning at 2 o'clock and 5 o'clock [5%], 4 o'clock [1%])
Fundus	1–2+ pallor, otherwise normal macula and vessels	1+ pallor, otherwise normal macula and vessels